

COMPUTATIONAL FLUID DYNAMICS SIMULATIONS OF HYDRAULIC ENERGY ABSORBER

by
Ya-Tien 'Mac' Chiu

Thesis submitted to the Faculty of the
Virginia Polytechnic Institute and State University
in partial fulfillment of the requirements for the degree of

MASTER OF SCIENCE
in
Mechanical Engineering

APPROVED:

P. S. King, Chairman

W. F. O'Brien

C. L. Dancey

July 21, 1999
Blacksburg, Virginia

Keywords: Computational Fluid Dynamics, CFD, Hydraulic, Energy Absorber

COMPUTATIONAL FLUID DYNAMICS SIMULATIONS OF HYDRAULIC ENERGY ABSORBER

by
Ya-Tien 'Mac' Chiu
Committee Chairman: Peter S. King
Mechanical Engineering

(ABSTRACT)

Hydraulic energy absorbers may be described as high-loss centrifugal turbomachines arranged to operate as stalled torque converters. The device absorbs the kinetic energy of a vehicle in motion and dissipates the energy into water. A steady, single-phase, Computational Fluid Dynamics (CFD) simulation has been performed to investigate the flow field in a hydraulic energy absorber. It was determined that to better predict the performance of the energy absorber, more sophisticated modeling approaches may be needed.

In this research, a steady, two-phase calculation with basic turbulence modeling was used as a first assessment. The two-phase model was used to investigate cavitation effects. Unsteady and advanced turbulence modeling techniques were then incorporated into single-phase calculations. The Multiple Reference Frame (MRF) Technique was used to model the interaction between the rotor and the stator. The calculations provided clearer details of the flow field without dramatically increasing the computational cost.

It was found that unsteady modeling was necessary to correctly capture the close coupling between the rotor and the stator. The predicted torque in the unsteady calculations was 70% of the experimental value and twice of the result in the steady-state calculations. It was found that the inaccuracy of torque prediction was due to (1) high pressures in the regions with complicated geometrical boundaries and, (2) dynamic interactions between the rotor and the stator were not captured fully. It was also determined that the unrealistically low pressure values were not caused by the physical cavitation, but by the lack of proper boundary conditions for the model. Further integration of the modeling techniques studied would improve the CFD results for use in the design of the energy absorber.

Acknowledgements

The author would like to take a moment to recognize some of the numerous who have contributed to this work. I would like to thank the members of this committee for serving in this capacity. I would like to specially thank Dr. Peter S. King for his immeasurable support and instructions. By giving me free reign and timely advice, I learned more in the self-propelled goal pursuing way than I could ask for. His friendship also helped me through some of the intricate difficulties when studying abroad and made this experience beyond my wonder. I would also like to thank Dr. Walter F. O'Brien for his advice, the turbomachinery knowledge he provided, and for introducing me to Dr. King. His counsel was most invaluable.

I would like to thank Christian Brothel for his fine work and assistance. He provided precious tuition and experiences of the FLUENT code when he was consumed by the completion of his own work. I would also like to thank Shaun Boller, Joe Howard, Scott Gallimore, Jeff Schwartz, and Maj. Keith Boyer (USAF) for their friendship. Technical support from Mary Kafura, Benjamin Poe, and Steve LePera and administrative assistance by Elloise McCoy and Cathy Hill are also greatly appreciated.

I would especially like to thank my parents for their support during my studies. Letting both of their children to fly across half of the world in pursuit of advanced education was not easy. I am proud that their resolution had strengthened mine and drove me toward the completion.

Last but not the least, there is one person that I am deeply indebted to, and that is my fiancée Jia-Huey. Her love and faith in me have never diminished by the great distance that separated us in this two years. Because she could not be with me to help me directly, she took up the responsibility to help and provide company to my parents to relieve my worries. Her understanding and consideration is a rarity for her age, I am most appreciated and I am in a live-debt to her.

Table of Contents

ABSTRACT	ii
ACKNOWLEDGEMENTS	iii
TABLE OF CONTENTS	iv
LIST OF FIGURES	vii
LIST OF TABLES	x
NOMENCLATURE	xi
1.0 INTRODUCTION	1
2.0 LITERATURE REVIEW	4
2.1 INTRODUCTION	4
2.2 AUTOMOBILE TORQUE CONVERTER STUDIES	4
2.3 BAFFLED MIXING TANK STUDIES	6
2.4 SUMMARY	9
3.0 NUMERICAL MODELING AND TECHNIQUES IN FLUENT	10
3.1 INTRODUCTION	10
3.2 TURBULENCE MODELS	10
3.2.1 REYNOLDS AVERAGING OF THE CONSERVATION EQUATIONS	11
3.2.2 THE k-ϵ TURBULENCE MODEL	13
3.2.3 THE REYNOLDS STRESS MODEL	15
3.3 SWIRLING AND ROTATING FLOWS MODEL	18
3.3.1 MULTIPLE REFERENCE FRAMES MODEL	18
3.3.2 SLIDING MESH MODEL	20
3.4 EULERIAN MULTIPHASE MODEL	23

4.0	SIMULATION SETUP	27
4.1	PRELIMINARY STUDY	27
4.2	STRUCTURED GRID GENERATION	28
4.2.1	GEOMETRY CONSIDERATIONS	29
4.2.2	GRID GENERATION	31
4.3	MODELING ASSUMPTIONS AND PARAMETERS	34
4.3.1	BASIC HYPOTHESIS	34
4.3.1.1	CAVITATION SIMULATION	35
4.3.1.2	UNSTEADY k-ϵ CALCULATION	36
4.3.1.3	UNSTEADY REYNOLDS STRESS MODEL CALCULATION	36
4.3.2	MODELING PARAMETERS	36
5.0	RESULTS AND DISCUSSIONS	38
5.1	INTRODUCTION	38
5.2	CAVITATION SIMULATION	39
5.2.1	OVERVIEW	39
5.2.2	GRAPHICAL RESULTS	40
5.3	UNSTEADY k-ϵ CALCULATION	44
5.3.1	OVERVIEW	44
5.3.2	GRAPHICAL RESULTS	44
5.4	UNSTEADY REYNOLDS STRESS MODEL CALCULATION	48
5.4.1	OVERVIEW	48
5.4.2	GRAPHICAL RESULTS	49
5.5	TORQUE CALCULATIONS	52
5.5.1	DYNAMIC TORQUE EFFECT	53
5.5.2	ADDITIONAL UNSTEADY TORQUE CALCULATIONS	56
5.5.3	EXPERIMENTAL DATA	59
5.6	PRESSURE DATA ANALYSIS	62
5.7	SUMMARY	71

6.0	CONCLUSIONS AND RECOMMENDATIONS	72
6.1	CONCLUSIONS	72
6.2	RECOMMENDATIONS	74
7.0	REFERENCES	76
8.0	APPENDIX A – STRUCTURED GRID DETAILS	79
9.0	APPENDIX B – REFINED STRUCTURED GRID	81
10.0	APPENDIX C – RESULTS OF THE CAVITATION SIMULATION	85
11.0	APPENDIX D – RESULTS OF THE UNSTEADY $k-\epsilon$ CALCULATION	97
12.0	APPENDIX E – RESULTS OF THE UNSTEADY RSM CALCULATION	108
VITA		119

List of Figures

Figure 1.1:	Geometrical features of the energy absorber.....	1
Figure 1.2:	Energy absorber in arresting system	2
Figure 1.3:	Predicted torque of Brothel’s result	3
Figure 2.1:	Geometrical features of the baffled mixing tank.....	7
Figure 3.1:	Physical and MRF representation of rotor/stator interaction	19
Figure 3.2a:	Initial position of the rotor and stator grids.....	21
Figure 3.2b:	Sliding of the rotor grid with respect to the stator grid	21
Figure 3.3:	Fictitious control volume treatment of slip surface.....	22
Figure 4.1a:	Computational blade shape	29
Figure 4.1b:	Actual blade shape	29
Figure 4.2:	Detail of the stator and the casing geometry	30
Figure 4.3:	Computational domain building.....	31
Figure 4.4:	Computational cell aspect ratio variation along radial direction.....	32
Figure 4.5:	Rotor surface grid.....	33
Figure 4.6:	Stator surface grid	33
Figure 5.1:	Dynamic torque comparison	54
Figure 5.2:	Torque comparison of the additional unsteady calculations	57
Figure 5.3:	Comparison of torque values with experimental data.....	60
Figure 5.4:	Pressure transducer locations	62
Figure 5.5:	Pressure data comparison: pressure side, 50% of stator blade length.....	65
Figure 5.6:	Pressure data comparison: suction side, 50% of stator blade length.....	65
Figure 5.7:	Pressure data comparison: pressure side, hub of stator blade	67
Figure 5.8:	Pressure data comparison: suction side, hub of stator blade	67
Figure 5.9:	Pressure data comparison: pressure side, tip of stator blade	68
Figure 5.10:	Pressure data comparison: suction side, tip of stator blade.....	68
Figure A.1:	Rotor grid detail	79
Figure A.2:	Stator grid detail.....	80
Figure B.1:	Refined rotor surface grid	81
Figure B.2:	Refined stator surface grid	82

Figure B.3:	Refined rotor grid detail	83
Figure B.4:	Refined stator grid detail	84
Figure C.1:	Contours of static pressure on the rotor	85
Figure C.2:	Contours of static pressure on the stator	86
Figure C.3:	Contours of volume fraction of water-vapor on the rotor	87
Figure C.4:	Contours of volume fraction of water-vapor on the stator	88
Figure C.5:	Contours of static pressure, 25% of the rotor blade length	89
Figure C.6:	Contours of static pressure, 50% of the rotor blade length	90
Figure C.7:	Contours of static pressure, 75% of the rotor blade length	91
Figure C.8:	Velocity vectors, 25% of the rotor blade length.....	92
Figure C.9:	Velocity vectors, 50% of the rotor blade length.....	93
Figure C.10:	Velocity vectors, 75% of the rotor blade length.....	94
Figure C.11:	Brothel's result: velocity vectors, 50% of the rotor blade length.....	95
Figure C.12:	Brothel's result: contours of static pressure on the rotor	96
Figure D.1:	Contours of static pressure on the rotor	97
Figure D.2:	Contours of static pressure on the stator	98
Figure D.3:	Contours of static pressure, 25% of the rotor blade length	99
Figure D.4:	Contours of static pressure, 50% of the rotor blade length	100
Figure D.5:	Contours of static pressure, 75% of the rotor blade length	101
Figure D.6:	Contours of static pressure, 99% of the rotor blade length	102
Figure D.7:	Contours of static pressure, interface region.....	103
Figure D.8:	Velocity vectors, 25% of the rotor blade length.....	104
Figure D.9:	Velocity vectors, 50% of the rotor blade length.....	105
Figure D.10:	Velocity vectors, 75% of the rotor blade length.....	106
Figure D.11:	Velocity vectors, interface region	107
Figure E.1:	Contours of static pressure on the rotor	108
Figure E.2:	Contours of static pressure on the stator	109
Figure E.3:	Contours of static pressure, 25% of the rotor blade length	110
Figure E.4:	Contours of static pressure, 50% of the rotor blade length	111
Figure E.5:	Contours of static pressure, 75% of the rotor blade length	112
Figure E.6:	Contours of static pressure, 99% of the rotor blade length	113

Figure E.7:	Contours of static pressure, interface region.....	114
Figure E.8:	Velocity vectors, 25% of the rotor blade length.....	115
Figure E.9:	Velocity vectors, 50% of the rotor blade length.....	116
Figure E.10:	Velocity vectors, 75% of the rotor blade length.....	117
Figure E.11:	Velocity vectors, interface region	118

List of Tables

Table 3.1:	Curvature-Related Source Terms in the RSM.....	16
Table 5.1:	Comparison of torque data after two full rotations	55
Table 5.2:	Physical properties comparison.....	56
Table 5.3:	Comparison of torque data after two full rotations	57
Table 5.4:	Comparison of viscous torque after two full rotations.....	58
Table 5.5:	Experimental and numerical values of the torque.....	59
Table 5.6:	Integration of the pressure differences	70

Nomenclature

C_D	Drag coefficient
d	Diameter of droplet/bubble
D_i	Diffusion coefficient of species i
F	External body force vector
g	Gravitational constant of acceleration
G_k	Rate of production of turbulent kinetic energy
G_b	Generation of turbulence due to buoyancy
\mathbf{i}_i	Orthogonal vectors in the Cartesian reference frame
J	Diffusive mass flux of species
k	Turbulent kinetic energy
K	Momentum exchange coefficient
\dot{m}	Mass transfer rate
M	Molecular weight
p	Pressure
p_v	Pressure of vaporization
r	Radius of droplet/bubble
\mathbf{r}	Position vector in the rotating frame of reference
Re	Reynolds Number
S_h	Energy source term
S_m	Mass source term
t	Time
T	Temperature
2D	Two-dimensional
3D	Three-dimensional
\mathbf{u}	Velocity vector
\mathbf{v}	Velocity vector in cylindrical reference frame
V	Volume
\mathbf{x}	Position vector

Acronyms

CFD	Computational Fluid Dynamic
MRF	Multiple Reference Frames
RNG	ReNormalization Group
RSM	Reynolds Stress Model

Greek Symbols

α	Volume fraction
δ	Kronecker delta
ε	Dissipation rate of the turbulent kinetic energy
μ	Molecular viscosity
Ω	Angular velocity vector
ω	Angular velocity magnitude
ρ	Density
σ	Lennard-Jones parameter
$\sigma_{k,\varepsilon}$	Prandtl number for turbulent quantities
$\tau_{i,j}$	Stress Tensor

Subscripts

i, j, k	Cartesian reference frame indexes
l	Summation index
t	turbulent
eff	effective
ref	reference
x	Axial direction
r, θ , z	Cylindrical reference frame indexes
p, q, r	Phase indexes

Superscripts

'	Turbulent quantities
---	----------------------

1.0 Introduction

A hydraulic energy absorber is a device that employs basic physical principles to absorb kinetic energy. By turning a rotor within a fluid-filled casing that contains stator blades, kinetic energy is transferred to heat and turbulent kinetic energy in the fluid. A major energy absorber application is in an arresting mechanism to stop a landing aircraft on the runway. Figure 1.1 below describes the main geometrical features of an arresting gear energy absorber in a common configuration.

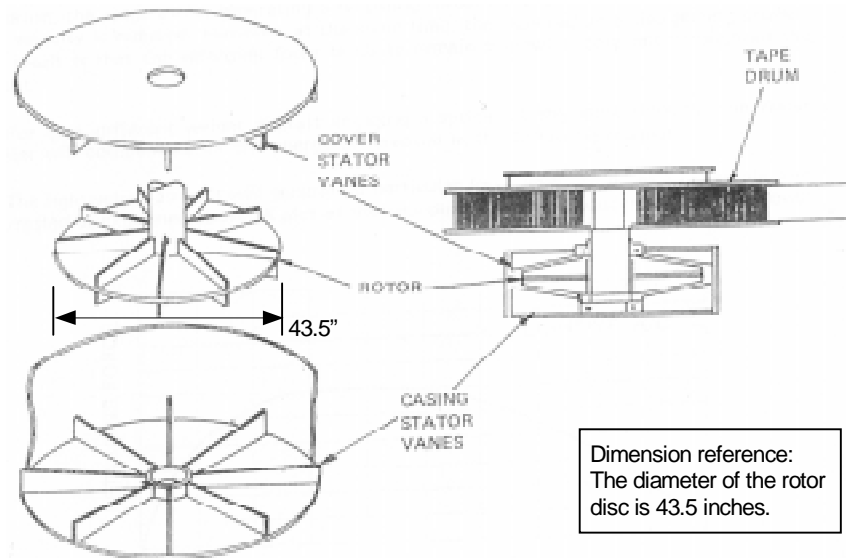


Figure 1.1 Geometrical features of the energy absorber

A nylon tape from the rotor shaft winds around the drum and then connects to an arresting cable on the runway. As the tailhook of an aircraft captures the cable during landing, the tape is pulled from the tape drum, causing the rotor to revolve. The motion of the rotor through the fluid generates a retarding force. The force decelerates the tape and thus the aircraft, and transfers vehicle momentum and kinetic energy away. The kinetic energy of the aircraft is then converted into heat and dissipated into the fluid in the energy absorber. Figure 1.2 illustrates the basic configuration of an arresting system utilizing the energy absorber.

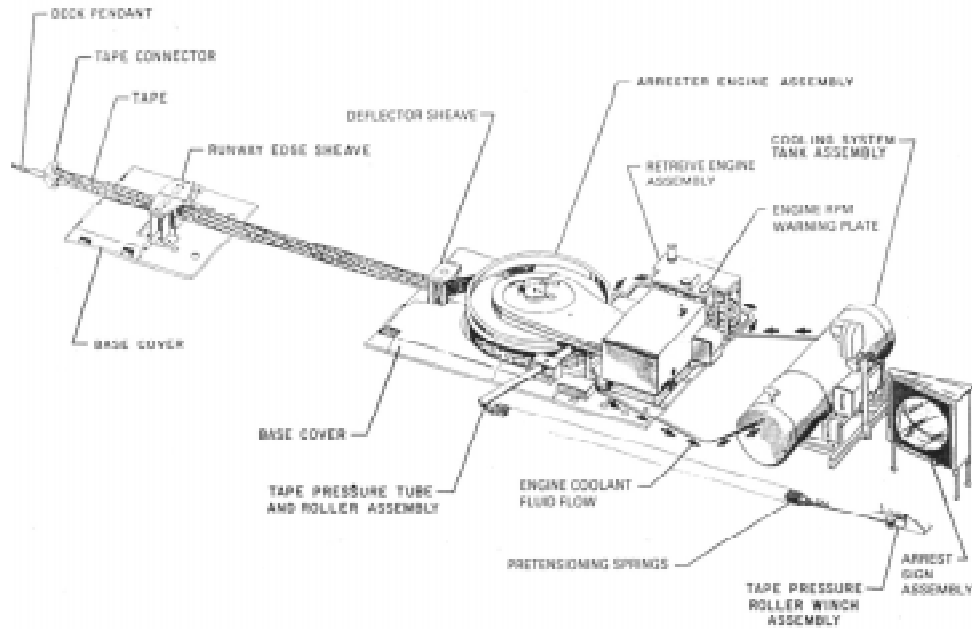


Figure 1.2 Energy absorber in arresting system

In order to accommodate a wider variety of aircraft for an arresting system, sufficient understanding of the internal flow and performance prediction of the energy absorber is required. However, due to the instantaneous nature of the process and the physical restriction in measuring the flow quantities in narrow rotating passages, accurate experimental data is extremely hard to obtain. Thus, analytical and computational modeling is introduced to provide an affordable investigation. This thesis addresses new discoveries from Computational Fluid Dynamics (CFD) simulations of the energy absorber.

The only previous work found for this particular energy absorber was done by Brothel [1] (1998); he employed FLUENT code to simulate the internal flow of the energy absorber. The calculation was done using an unstructured grid and employed the standard $k-\epsilon$ turbulence model and the Sliding Mesh Technique, assuming steady state and a single-phase fluid. Some characteristics of the complex flow field were captured by the steady-state approximation, but the result fell short in predicting the rotor torque values. Figure 1.3 shows the comparison of his predicted torque and the experimental values.

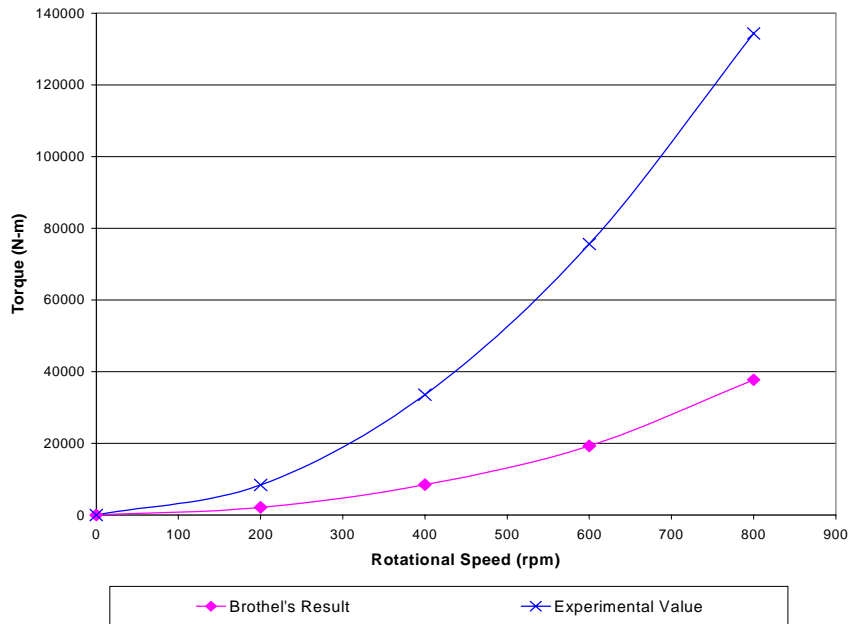


Figure 1.3 Predicted torque of Brothel's result

One can see from Figure 1.3 that the CFD predicted torque was only about 30% of the experimental value. Another problem with the result was that unrealistically low pressures were present. It was concluded that different modeling methods and assumptions, especially a different turbulence model and a cavitation simulation, should be considered for future investigations.

In Chapter 2 of this thesis, previous CFD research in similar applications is reviewed. Chapter 3 addresses the mathematical models and numerical methods in the FLUENT code and their limitations, while preliminary calculations and simulation setup are presented in Chapter 4. Chapter 5 discusses the CFD results employing specific modeling techniques. Conclusions and recommendations for future work are presented in Chapter 6.

2.0 Literature Review

2.1 INTRODUCTION

The advances in computer technology have improved the capability of CFD simulation dramatically in recent years and it has become instrumental in a wide range of applications. However, the current state of numerical modeling methods still demands considerable amounts of computational labor in hydrodynamics, and hinders the utilization of CFD in an arena that still dominated by empirical methods. As has been mentioned previously, the only investigation found on the specific energy absorber under consideration was done by Brothel in 1998. No research in regard to other energy absorbers or hydraulic turbomachinery with similar geometry was found.

Because the energy absorber can be described as a stalled torque converter, some research reports regarding automobile torque converters were found. Their geometrical features and flows were different, but some common points with the energy absorber exist. Furthermore, CFD modeling of gas-liquid flow in a stirred mixing vessel has been investigated, often in conjunction with experimental comparison. The interactions between impeller and baffle blades are similar to the coupling of rotor and stator blades in the energy absorber, to some extent; the experience from these simulations provides useful insight into the difficulties in simulating the energy absorber flows.

2.2 AUTOMOBILE TORQUE CONVERTER STUDIES

The configuration of a typical automotive torque converter consists of a pump driven by an input shaft, a turbine driving an output shaft and a stator blade disc that may freewheel forward but is prevented from rotating backwards by a one-way clutch. An automotive torque converter typically produces an output torque that changes smoothly from two to three times the input torque at stall (zero turbine speed) to a torque equal to the input torque at the coupling point.

One-dimensional streamline theory is often implemented in the method to design an automobile torque converter. Empirical means are then employed to calculate flow losses based on actual performance data obtained from previously built torque converters. The process is successful and useful in new designs with similar geometry, but far from satisfactory in performance prediction if a new geometry is applied. Both experimental and numerical studies have been done in the effort to reconstruct the complex internal flow within the torque converter, and the investigations have revealed some of the main features of the flow field.

Numazawa, et al. [2] (1983) developed an oil-film-resin flow visualization technique to trace flow patterns on the blade and end-wall surfaces. They employed the technique and visualized crossflow, swirl, reversed flow, and separated flows in the torque converter. The geometry profile was then modified based on theoretical predictions of pressure distributions in order to obtain smoother flows, and then a higher efficiency torque converter was developed.

Fujitani, et al. [3] (1988) solved the Navier-Stokes equations for the pump, turbine and stator of an automotive torque converter. They coupled the three elements so that they could evaluate the torque converter performance without empirical parameters or measured data. This study demonstrated the possibility of employing numerical simulations in the design of torque converter.

Bahr, et al. [4] (1990) employed a laser velocimeter (LV) in a Plexiglas torque converter to obtain detailed velocity profiles of five planes in the stator. Laser velocimetry provides 3-D details of the flow in small rotating passages without changing the flow field. Unsteady separation regions and circulatory secondary flows were observed and the research provided improved flow visualization by eliminating the disturbance of instrumentation.

By and Lakshminarayana [5] (1991) performed analytical modeling and experimental validations using the same geometry as Bahr, et al. Their results showed that the primary factor on the static pressure rise in the pump is the centrifugal force, and the static pressure distribution is generally poor at the blade core section. The velocity gradients coupled with flow turning induced strong secondary flows that dominated the flow field in the torque converter. They also demonstrated that potential flow theory could be applied in predicting the static pressure distribution at the blade mid span with sufficient accuracy, but not at the core and shell sections.

Abe, et al. [6] (1991) found that the pump rotation has a major effect on the secondary flow field and that the inlet velocity profile dominates the total pressure loss. The Navier-Stokes calculations done by Abe, et al. were employed by By, et al. [7] (1993). They developed a three-dimensional, incompressible, viscous flow code to predict the flow field in a torque converter pump and confirmed the work of Abe, et al.

Schulz, Greim, and Volgmann [8] (1994) used a finite volume method in calculating three-dimensional, incompressible turbulent flow. Both steady state and unsteady state calculations to simulate the pump/turbine interactions were performed. Their calculations showed that unsteady interaction of the stator with the pump or turbine was negligible, but needed to be accounted for in the region between the pump and the turbine. Although they were content with the results, they stressed that viscous effects were not fully captured and the turbulence modeling had to be improved.

2.3 BAFFLED MIXING TANK STUDIES

Baffled mixing tanks are often found in the form of gas-liquid mixers used in various industries. Their configuration usually consists of a shaft with rotating impeller blades and baffles on the surface of the containing vessel. Figure 2.1 shows the basic geometry of a baffled mixing tank.

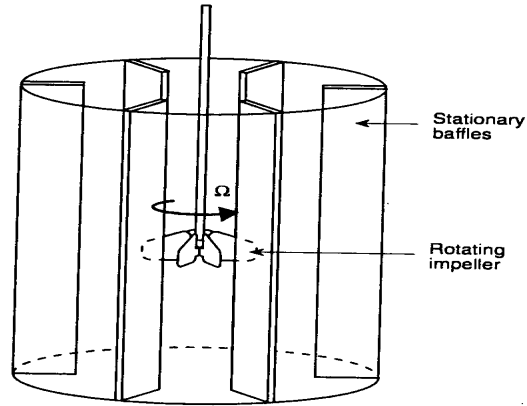


Figure 2.1 Geometrical features of the baffled mixing tank

Due to the various applications in use, many investigations of baffled mixing tanks have been performed and have achieved different degrees of success. The mixing process of the device demands the implementation of a two-phase modeling technique. Both Lagrangian and Eulerian approaches for two-phase treatment have been utilized depending on the concentration of the gas phase. However, single-phase approximations are not uncommon in order to reduce the computational cost. Most calculations employ standard $k-\varepsilon$ turbulence models in order to reduce the computational difficulty of advanced turbulence modeling.

Placek and Tavlarides [9, 10] (1985, 1986) predicted and measured the flow patterns and turbulence properties in a two-dimensional baffled vessel. They applied a three-equation turbulence model and assumed anisotropic turbulence in the impeller region. They found that different results were obtained based on different assumptions concerning the impeller boundary and concluded that the two-dimensional model could provide sufficient approximation with appropriate impeller boundary treatment.

Torvik and Svendsen [11] (1990) developed a dynamic two-phase model incorporating a $k-\varepsilon$ turbulence model, a compressible gas phase and axisymmetry based on fundamental “first principles”. Their predicted gas fraction profiles are in qualitative agreement with local gas fraction measurements. However, they also found that simulated values of turbulent kinetic energy are well below the measured values due to the inadequacy of the $k-\varepsilon$ turbulence model.

Kresta and Wood [12] (1991) developed an analytical model that combined the swirling radial jet model and the k - ε turbulence model to obtain the turbulent parameters at the tip of the impeller. The data were then used as boundary conditions in the three-dimensional single-phase calculations with the k - ε turbulence model using the FLUENT code to simulate a tank without inlet and outlet. Their simulations yield satisfactory agreement with experimental results. They concluded that the calculations done with the k - ε turbulence model could be improved with better boundary conditions when more sophisticated turbulence model is not available.

Gosman, et al. [13] (1992) employed a two-fluid Eulerian model and extended the single-phase k - ε turbulence model to two-phase flow. Using the new model, they performed liquid-gas flow simulations in a three-dimensional calculation domain. Their results produced physically realistic predictions and agreed qualitatively with experimental data. However, they indicated that testing of the model in various operating conditions and improvement in describing boundary conditions is necessary before the method can be established as a reliable design tool.

Takeda, et al. [14] (1993) modeled single-phase flow in a stirred tank where both the impeller and the baffle were taken as part of the reactor boundary. They used the RFLOW code that provided a dynamic multi-block method with rotating coordinates for the inner block and fixed coordinates for the outer block. It was shown that the velocity transient across the interface was smooth and the results provided high-quality visualization of the unsteady velocity field within the tank.

Morud and Hjertager [15] (1996) performed simulations using a two-dimensional, two-fluid model with a standard k - ε turbulence model. The impellers and baffles were modeled by introducing source and sink terms in the appropriate momentum equations. They also used a laser/phase Doppler anemometer (LDA/PDA) to measure the gas velocities of the mixture and validated the estimation of the CFD calculations.

2.4 SUMMARY

One can find that the three-dimensional, viscous and unsteady flow fields of both applications have been studied in order to develop new design methods. The torque converter currently under study has strong interactions between rotor and stator due to the close confines of parts, while a baffled mixing tank has moderate interaction but is complicated by the presence of second phase. However, the complexity of the flows within them has limited the ability of CFD simulations to model both applications, and the industry still prefers empirical methods to numerical ones. Different techniques have been introduced in order to increase the fidelity of unsteady 3-D CFD calculations, but successes are usually limited to certain operating conditions and simpler geometries.

The flow field within the energy absorber of this research presents a greater challenge than both applications because stronger interactions are expected and simulating the possible cavitation is more difficult than simulating the pure two-phase mixing process. It is apparent from the experiences of these studies that the integration of advanced modeling techniques as well as sophisticated experimental validation is needed to fully capture the complex flows in the energy absorber. However, experimental and numerical studies of the energy absorber are not enough at the current stage. In this study, different CFD modeling techniques are tested in order to obtain results that better match the experimental pressure and torque data. It is hoped that by comparing the degree of success in each simulation, a better understanding of the physical phenomenon within the flow field can be achieved and a combination of these techniques can be found that optimizes the accuracy of the result and the computational cost.

3.0 Numerical Modeling and Techniques in FLUENT

3.1 INTRODUCTION

The concept of Computational Fluid Dynamics (CFD) is to utilize the computer in the numerical calculation of a complex mathematical model. The differential equations of motion are transformed to a large number of algebraic equations. The solution is generated from intensive iteration of these equations made possible only by the computer. In order to obtain acceptable results, an understanding of the characteristics of the flow field as well as the theoretical model being applied is necessary. This study uses the FLUENT [16] package, a commercial CFD code, to investigate the internal flow of an energy absorber. The basic mathematical model of FLUENT includes the fundamental conservation equations for laminar flow to accommodate both Newtonian and Non-Newtonian flow. Different subroutines are called if the user enables different modeling methods to represent the physics of the flow field.

As described earlier, the close coupling of the moving elements in the geometry requires the careful consideration of turbulence models, modeling of the interface between rotating and stationary regions, and the two-phase model if cavitation is suspected. However, the theoretical model that best describes the problem on paper may be a poor choice because of the computational cost. Detailed examination of the capability of each model is needed and the choice of technique requires wise engineering judgement. The theoretical origin of the models in FLUENT is addressed thoroughly in the manual [17]. This chapter presents refined excerpts of these discussions about the techniques used in the simulations and their limitations.

3.2 TURBULENCE MODELS

Modeling of turbulent flows requires appropriate modeling procedures to describe the effect of the turbulent fluctuation of velocity and scalar quantities on the basic

conservation equations. [17] While direct simulation of turbulence is currently studied at a research level, FLUENT closes the equation set via time-averaging procedures and closure models.

3.2.1 Reynolds Averaging of the Conservation Equations

The Reynolds averaging procedure [18] for scalar equations can be illustrated using a generic transport equation for a conserved scalar quantity ϕ .

$$\underbrace{\frac{\partial}{\partial t}(\rho\phi)}_{\text{Accumulation}} + \underbrace{\frac{\partial}{\partial x_i}(\rho u_i \phi)}_{\text{Convection}} = \underbrace{D_\phi}_{\text{Diffusion}} + \underbrace{S_\phi}_{\text{Source}} \quad 3.2-1$$

The value of ϕ in turbulent flows is assumed to be comprised of a mean value and a fluctuating part

$$\phi = \bar{\phi} + \phi' \quad 3.2-2$$

where $\bar{\phi}$ is the time-averaged value of ϕ defined as

$$\bar{\phi} = \frac{1}{\Delta t} \int_t^{t+\Delta t} \phi dt \quad 3.2-3$$

and Δt is a time scale much larger than the largest time scale of turbulent fluctuations. Turbulent fluctuations ϕ' are assumed to be random such that

$$\bar{\phi}' = 0 \quad 3.2-4$$

Substitution of equation 3.2-2 into the general conservation equation 3.2-1 and integration over a sufficiently large time interval yields

$$\frac{\partial}{\partial t}(\bar{\rho}\bar{\phi}) + \frac{\partial}{\partial x_i}(\bar{\rho}\bar{u}_i\bar{\phi}) = -\frac{\partial}{\partial x_i}(\bar{\rho}\overline{u'_i\phi'}) + \bar{D}_\phi + \bar{S}_\phi \quad 3.2-5$$

This result assumes that the density fluctuations are negligible. In all following equations, the overbar will be dropped from the averages quantities for the sake of convenience. The terms in equation 3.2-5 are similar to those in its laminar flow counterpart, except that

each quantity now is represented by its time averaged value and a new term containing the correlation $\overline{u'_i \phi'}$ appears on the right-hand side. Physically, this correlation multiplied by the density represents the transport "diffusion" of ϕ due to the turbulent fluctuation.

In the Reynolds averaging of the momentum equations, the velocity at a point is considered as a sum of the mean (time averaged) and fluctuating components

$$u_i = \bar{u}_i + u'_i \quad 3.2-6$$

Substituting expressions of this form into the basic momentum balance yields the ensemble-averaged momentum equations for predicting turbulent flows

$$\begin{aligned} \frac{\partial}{\partial t}(\rho u_i) + \frac{\partial}{\partial x_j}(\rho u_i u_j) = \frac{\partial}{\partial x_j} \left(\mu \left[\frac{\partial u_i}{\partial x_j} + \frac{\partial u_j}{\partial x_i} \right] - \left(\frac{2}{3} \mu \frac{\partial u_l}{\partial x_l} \right) \right) \\ - \frac{\partial p}{\partial x_i} + \rho g_i + F_i + \frac{\partial}{\partial x_j} \left(- \overline{\rho u'_i u'_j} \right) \end{aligned} \quad 3.2-7$$

Equation 3.2-7 has the same form as the fundamental momentum balance with velocities now representing time-averaged (or mean-flow) values and the effect of turbulence incorporated through the "Reynolds Stresses", $\overline{\rho u'_i u'_j}$. Note that $\overline{u'_i u'_j}$ is a symmetric second order tensor since

$$\overline{u'_i u'_j} = \overline{u'_j u'_i} \quad 3.2-8$$

and hence has six unique terms.

Due to the complexity of the equations above, a complete knowledge of those new variables cannot be obtained; this is defined as the closure problem of the Reynolds time-averaged equations. The main task of turbulence modeling is to provide expressions, or closure models, that allow the evaluation of these correlations in terms of mean flow quantities. There is a wide range of different turbulence closure models available and new modeling are being developed as well; some models are suitable to some types of flows, while some others do not correctly predict the effects of walls or circulating flows. The

turbulence models provided by FLUENT include the k - ε model, the ReNormalization Group k - ε model (RNG) and the Differential Reynolds Stress Model (RSM). The two models used in this research are described in the next section.

3.2.2 The k - ε Turbulence Model

The k - ε Turbulence Model is an eddy-viscosity model in which the Reynolds stresses are assumed to be proportional to the mean velocity gradients, with the constant of proportionality being the turbulent viscosity, μ_t . This assumption, known as the Boussinesq hypothesis, provides the following expression for the Reynolds stresses [18]

$$\overline{\rho u_i u_j} = \rho \frac{2}{3} k \delta_{ij} - \mu_t \left(\frac{\partial u_i}{\partial x_j} + \frac{\partial u_j}{\partial x_i} \right) + \frac{2}{3} \mu_t \frac{\partial u_i}{\partial x_i} \delta_{ij} \quad 3.2-9$$

Here k is the turbulent kinetic energy defined by

$$k = \frac{1}{2} \sum_i \overline{u_i^2} \quad 3.2-10$$

Equation 3.2-9 for the Reynolds stresses is analogous to that describing the shear stresses that arise in laminar flow (Equation 3.2-3), with the turbulent viscosity μ_t playing the same role as the laminar viscosity μ . Therefore, the form of the Reynolds averaged momentum equations remains identical to that of the molecular momentum equations (Equation 3.2-2), except that μ is replaced by the effective viscosity, μ_{eff} , where

$$\mu_{eff} = \mu + \mu_t \quad 3.2-11$$

The turbulent viscosity μ_t is obtained by assuming that it is proportional to the product of a turbulent velocity scale and length scale. In the k - ε model, these velocity and length scales are obtained from two parameters: k , the turbulent kinetic energy and ε , the dissipation rate of k .

The velocity scale is taken to be \sqrt{k} and the length scale is taken to be $\frac{\sqrt{k^3}}{\varepsilon}$.

Hence, μ_t is given by

$$\mu_t = \rho C_\mu \frac{k^2}{\varepsilon} \quad 3.2-12$$

where C_μ is an empirically derived constant of proportionality (set to a default value of 0.09 usually).

The values of k and ε required in Equation 3.2-12 are obtained by solution of the conservation equations [19]

$$\frac{\partial}{\partial t}(\rho k) + \frac{\partial}{\partial x_i}(\rho u_i k) = \frac{\partial}{\partial x_i} \left(\frac{\mu_t}{\sigma_k} \frac{\partial k}{\partial x_i} \right) + G_k + G_b - \rho \varepsilon \quad 3.2-13$$

$$\frac{\partial}{\partial t}(\rho \varepsilon) + \frac{\partial}{\partial x_i}(\rho u_i \varepsilon) = \frac{\partial}{\partial x_i} \left(\frac{\mu_t}{\sigma_\varepsilon} \frac{\partial \varepsilon}{\partial x_i} \right) + C_{1\varepsilon} \frac{\varepsilon}{k} (G_k + (1 - C_{3\varepsilon}) G_b) - C_{2\varepsilon} \rho \frac{\varepsilon^2}{k} \quad 3.2-14$$

where $C_{1\varepsilon}$, $C_{2\varepsilon}$ and $C_{3\varepsilon}$ are empirical constants, σ_k and σ_ε are ‘‘Prandtl’’ numbers governing the turbulent diffusion of k and ε , G_k is the rate of production of turbulent kinetic energy

$$G_k = \mu_t \left(\frac{\partial u_j}{\partial x_i} + \frac{\partial u_i}{\partial x_j} \right) \frac{\partial u_j}{\partial x_i} \quad 3.2-15$$

and G_b is generation of turbulence due to buoyancy:

$$G_b = -g_i \frac{\mu_t}{\rho \sigma_h} \frac{\partial \rho}{\partial x_i} \quad 3.2-16$$

The coefficients $C_{1\varepsilon}$, $C_{2\varepsilon}$, C_μ , σ_k and σ_ε are empirical constants and the following empirically derived values are often used [20]:

$$C_{1\varepsilon} = 1.44, \quad C_{2\varepsilon} = 1.92, \quad C_\mu = 0.09, \quad \sigma_k = 1.0, \quad \sigma_\varepsilon = 1.3$$

One of the weaknesses of conventional eddy-viscosity models is that production of turbulent kinetic energy, G_k , in Equation 3.2-15 results in excessive turbulence energy in regions where the mean flow is highly accelerated or decelerated. The erroneously high level of turbulent kinetic energy typically suppresses flow separation and subsequent vortex shedding, if any, downstream of the stagnation point. The problem originates from the way in which the production term is modeled in the eddy-viscosity-based models. Irrotational strains appearing in Equation 3.2-15 always generates turbulence regardless of their sign, while, in reality, they may sometimes suppress turbulence. Kato and Launder have proposed to include the mean vorticity tensor in the expression for the production, which will remove, as an alternative way of computing the production term, the contribution from irrotational strains.

The semi-empirical k- ϵ mode has been proven to provide engineering accuracy in a wide variety of turbulent flows including flows with planar shear layers such as jet flows, duct flows, etc. However, the k- ϵ model adopts an isotropic description of the turbulence through μ_t , as described above, and is thus not well suited for flows in which anisotropy of turbulence significantly affects the mean flow. For some cases, the ReNormalization Group k- ϵ model (RNG) and the Differential Reynolds Stress Model (RSM) models yield better results compared with the standard k- ϵ model, but the simplicity and versatility in regard to computational effort still makes it an appealing choice in the early stages of any simulation.

3.2.3 The Reynolds Stress Model

The Reynolds Stress Model (RSM) involves solving the transport equations for the individual stresses $\overline{u_i u_j}$ appearing in Equation 3.2-8. These transport equations can be derived from the momentum equations and contain triple order velocity correlations and pressure velocity correlations that must be modeled to obtain closure. The following equations that are based on the modeling assumption of references [21] and [22] are used by the RSM of FLUENT:

$$\begin{aligned}
& \underbrace{\frac{\partial}{\partial t} (\overline{u_i u_j}) + u_k \frac{\partial}{\partial x_k} (\overline{u_i u_j})}_{\text{Convective Transport}} = - \underbrace{\frac{\partial}{\partial x_k} \left[(\overline{u_i u_j u_k}) + \frac{p'}{\rho} (\delta_{kj} u_i + \delta_{ik} u_j) - \nu \frac{\partial}{\partial x_k} (\overline{u_i u_j}) \right]}_{\text{Diffusive Transport}} \\
& - \underbrace{\left[\overline{u_i u_k} \frac{\partial u_j}{\partial x_k} + \overline{u_j u_k} \frac{\partial u_i}{\partial x_k} \right]}_{P_{ij} = \text{Production}} + \underbrace{\frac{p'}{\rho} \left[\frac{\partial u_i}{\partial x_j} + \frac{\partial u_j}{\partial x_i} \right]}_{\phi_{ij} = \text{Pressure-Strain}} \\
& - 2\nu \underbrace{\left[\frac{\partial u_i}{\partial x_k} \frac{\partial u_j}{\partial x_k} \right]}_{\varepsilon_{ij} = \text{Dissipation}} - 2\Omega_k \underbrace{\left[\overline{u_j u_m} \varepsilon_{ikm} + \overline{u_i u_m} \varepsilon_{jkm} \right]}_{R_{ij} = \text{Rotational Term}} + \underbrace{S_{ij} + D_{ij}}_{\text{Curvature-Related Terms}}
\end{aligned} \tag{3.2-17}$$

where S_{ij} and D_{ij} are curvature-related source terms that are included when the cylindrical velocity formulation is used. Values for S_{ij} and D_{ij} are listed in Table 3.1. The individual Reynolds stresses are then substituted into the turbulent flow momentum equation. (Equation 3.2-7)

Table 3.1 Curvature-Related Source Terms in the RSM

ij	S_{ij}	D_{ij}	
		algebraic	differential
xx	—	—	—
xr	$\rho \frac{v_\theta}{r} \overline{v'_x v'_\theta}$	$-\overline{v'_x v'_r} \frac{\mu_t}{r^2}$	$-B \overline{v'_x v'_\theta}$
$x\theta$	$-\rho \frac{v_\theta}{r} \overline{v'_x v'_r}$	$-\overline{v'_x v'_\theta} \frac{\mu_t}{r^2}$	$B \overline{v'_x v'_r}$
rr	$2\rho \frac{v_\theta}{r} \overline{v'_r v'_\theta}$	$-2(\overline{v_r'^2} - \overline{v_\theta'^2}) \frac{\mu_t}{r^2}$	$-2B \overline{v'_r v'_\theta}$
$r\theta$	$\rho \frac{v_\theta}{r} (\overline{v_\theta'^2} - \overline{v_r'^2})$	$-4\overline{v'_r v'_\theta} \frac{\mu_t}{r^2}$	$B(\overline{v_r'^2} - \overline{v_\theta'^2})$
$\theta\theta$	$-2\rho \frac{v_\theta}{r} \overline{v'_r v'_\theta}$	$2(\overline{v_r'^2} - \overline{v_\theta'^2}) \frac{\mu_t}{r^2}$	$2B \overline{v'_r v'_\theta}$

$$B \equiv \left(\frac{1}{r^2} \partial_\theta \mu_t \right) + \frac{2\mu_t}{r^2} \partial_\theta$$

Several terms in Equation 3.2-17 need to be approximated in order to close the equation set. First, the diffusive transport term is described using a scalar diffusion coefficient [21]:

$$-\underbrace{\frac{\partial}{\partial x_k} \left[\overline{(u'_i u'_j u'_k)} + \frac{p'}{\rho} (\delta_{kj} u'_i + \delta_{ik} u'_j) - \nu \frac{\partial}{\partial x_k} \overline{(u'_i u'_j)} \right]}_{\text{DiffusiveTransport}} = \frac{\partial}{\partial x_k} \left(\frac{\nu_t}{\sigma_k} \frac{\partial \overline{(u'_i u'_j)}}{\partial x_k} \right) \quad 3.2-18$$

This approximation, with the assumption of isotropy of turbulence, is derived from a generalized gradient diffusion hypothesis by Daly and Harlow [23]. An alternative approximation is also available to account for anisotropy in the diffusive transport.

$$-\underbrace{\frac{\partial}{\partial x_k} \left[\overline{(u'_i u'_j u'_k)} + \frac{p'}{\rho} (\delta_{kj} u'_i + \delta_{ik} u'_j) - \nu \frac{\partial}{\partial x_k} \overline{(u'_i u'_j)} \right]}_{\text{DiffusiveTransport}} = \frac{\partial}{\partial x_l} \left(C_s \frac{k \overline{u'_l u'_l}}{\varepsilon} \frac{\partial \overline{(u'_i u'_j)}}{\partial x_l} \right) \quad 3.2-19$$

The second approximation in Equation 3.2-17 is for the pressure-strain term, which is approximated as

$$\underbrace{\frac{p'}{\rho} \left[\frac{\partial u'_i}{\partial x_j} + \frac{\partial u'_j}{\partial x_i} \right]}_{\phi_{ij} = \text{Pressure-Strain}} = -C_1 \frac{\varepsilon}{k} \left[\overline{(u'_i u'_j)} - \frac{2}{3} \delta_{ij} k \right] - C_2 \left[P_{ij} - \frac{2}{3} \delta_{ij} P - S_{ij} \right] + \phi_{ij}^w \quad 3.2-20$$

where C_1 and C_2 are empirical constants whose values are $C_1 = 1.8$ and $C_2 = 0.60$, and $P = \frac{1}{2} P_{ii}$.

The final approximation to Equation 3.2-17 is the dissipation term. It is assumed to be isotropic and is approximated by the scalar dissipation rate [24]:

$$2\nu \left[\frac{\partial u'_i}{\partial x_k} \frac{\partial u'_j}{\partial x_k} \right] = \frac{2}{3} \delta_{ij} \varepsilon \quad 3.2-21$$

The dissipation rate, ε , is computed via Equation 3.2-14. If directional diffusivity option (Equation 3.2-19) is used, the ε transport equation becomes [25]

$$\frac{\partial}{\partial t}(\rho\varepsilon) + \frac{\partial}{\partial x_i}(\rho u_i \varepsilon) = \frac{\partial}{\partial x_i} \left(C_\varepsilon \frac{\rho k}{\varepsilon} \overline{u_i u_i} \frac{\partial \varepsilon}{\partial x_i} \right) + C_{1\varepsilon} \frac{\varepsilon}{k} G_k - C_{2\varepsilon} \rho \frac{\varepsilon^2}{k} \quad 3.2-22$$

where $C_\varepsilon = 0.18$ and $G_k = \frac{1}{2} \rho P_{ii}$.

The RSM creates a high degree of tight coupling between the momentum equations and the turbulent stresses in the flow and is more appropriate in modeling complex flow where assumption of isotropic turbulence used in the k - ε model is inaccurate. However, additional equations (6 in 3-D calculation) have to be solved and the numerical scheme is more prone to stability and convergence difficulties than the k - ε model. Also, the RSM in FLUENT is compatible with the Sliding Mesh Techniques only when the grid is unstructured, which requires additional computational resources when the computational labor for former two techniques are already demanding.

3.3 SWIRLING AND ROTATING FLOWS MODEL

Swirling and rotating flows creates a unique set of flow physics for which special input requirements and solution techniques must be applied. Problems involving interaction of rotor/stator or impeller in a baffled tank requires additional treatment and FLUENT provides two different modeling techniques to simulate the flow field.

3.3.1 Multiple Reference Frames Model

In FLUENT, the Multiple Reference Frames (MRF) option was developed as an alternative to the sliding mesh approach for modeling flow field in geometry where there are parts that rotate relative to each other. Fluid motion in a rotating subdomain is solved in a rotating frame, and the solution is matched at the interface between the rotating and stationary regions via velocity transformations from one frame to the other. The “velocity matching” step implicitly involves the assumption of steady flow conditions at the

interface, but permits multiple fluid (not grid) regions to rotate relative to each other. Figure 3.1 illustrates a basic MRF modeling of rotor/stator interaction.

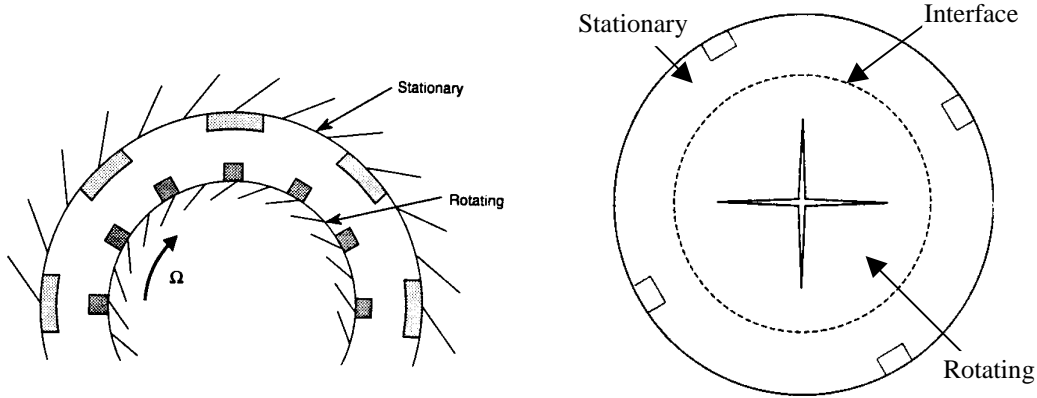


Figure 3.1 Physical and MRF representation of rotor/stator interaction

The equations of the rotating reference frame are revised momentum equations that introduce coriolis and centrifugal acceleration terms:

$$\frac{Dv_r}{Dt} + 2\Omega \times v_r + \Omega \times (\Omega \times r) \quad 3.3-1$$

Here, v_r is the velocity in the rotating frame and is related to the velocity in the non-rotating frame, v , as:

$$v = v_r + \Omega \times r \quad 3.3-2$$

where Ω is the rotation vector and r is the position vector in the rotating frame.

Since most applications involving swirling and rotating flows have some symmetry with respect to an axis of rotation, a cylindrical coordinate system is often applied in such simulations. The centrifugal acceleration term, $\Omega \times (\Omega \times r)$, when written in a cylindrical coordinate system, leads to the following force in radial direction:

$$\rho r_1 \Omega^2 \quad 3.3-3$$

The Coriolis term, $2\rho\Omega \times v_r$, yields a force in the circumferential direction:

$$2\rho\Omega v_r \quad 3.3-4$$

At the boundary between the rotating subdomain and the fixed laboratory frame, the continuity of the absolute velocity v needs to be enforced to provide correct neighbor values of velocity. Velocities in each subdomain are first computed relative to the motion of the subdomain. After the momentum equations have been updated, velocities and velocity gradients are converted to the absolute inertial frame as described below.

The position vector relative to the origin of the rotating frame is defined as

$$r = x - x_0 \tag{3.3-5}$$

where x is the position in absolute Cartesian coordinates and x_0 is the origin of the rotating frame. The relative velocity in the rotating reference frame can be obtained from the absolute frame of reference using Equation 3.3-2, and the velocity gradient is obtained using:

$$\nabla v = \nabla v_r + \nabla(\Omega \times r) \tag{3.3-6}$$

The MRF approach is an approximation implemented with reducing computational effort in mind. The assumption of a steady flow condition at the interface is best suited to situations where relatively weak interactions can be found, such as baffled mixing tank with enough spacing between the impellers and baffles. To represent the flow field where strong rotor/stator interaction occurs, such as the energy absorber under consideration, the Sliding Mesh model is necessary.

3.3.2 Sliding Mesh Model

The Sliding Mesh model approach involves two grid regions, one attached to a rotating geometry and the other attached to the stationary boundaries of the flow, which slide relative to one another along a slip plane. Figure 4.1 demonstrates the principle of the Sliding Mesh technique applied to a rotor and a stator mesh. As the rotation takes place, alignment of the two grids along the slipping surface to make the overall grid structured is no longer required. An arbitrary Lagrangian-Eulerian (ALE) method is used

to describe the general transport equations in both of the grid regions. Since the flow is inherently unsteady, a time-dependent solution procedure must be used.

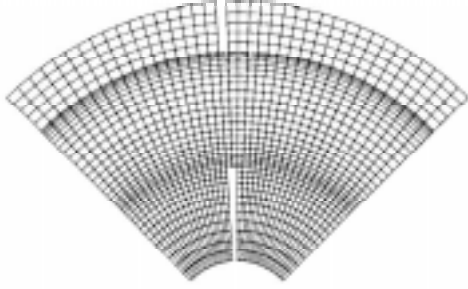


Figure 3.2a
Initial position of the rotor and stator grids

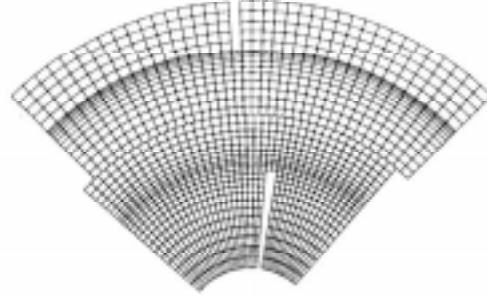


Figure 3.2b
Sliding of the rotor grid with respect to the stator grid

Because the Sliding Mesh model allows a moving grid region to slide relative to the stationary grid and does not demand the alignment of grid lines on the slip surface, a conservative interpolation is necessary to provide flow variables and face fluxes across the interface. The governing equations for the flows in the reference frame of the moving mesh may be written in Cartesian tensor form as [26]

$$\frac{1}{J} \frac{d}{dt} \rho J + \frac{\partial}{\partial x_j} (\rho u_j - v_j) = 0 \quad 3.3-7$$

$$\frac{1}{J} \frac{d}{dt} \rho J u_i + \frac{\partial}{\partial x_i} \rho (u_j - v_j) u_j = - \frac{\partial p}{\partial x_i} + \frac{\partial}{\partial x_j} (\tau_{ij} + \tau_{t,ij}) + S_{u_i} \quad 3.3-8$$

$$\frac{1}{J} \frac{d}{dt} \rho J \phi + \frac{\partial}{\partial x_j} \rho (u_j - v_j) \phi = \frac{\partial}{\partial x_j} \Gamma_\phi \frac{\partial \phi}{\partial x_j} + S_\phi \quad 3.3-9$$

where ρ is the fluid density

u_j is the flow velocity component

v_j is the grid velocity component arising from mesh motion

τ_{ij} is the molecular stress tensor for Newtonian fluids

$\tau_{t,ij}$ is the Reynolds stress tensor

Γ_ϕ is the diffusion coefficient for the scalar quantity ϕ

S_{u_i} is the source term for the u_i equation

S_ϕ is the source term for the ϕ equation

These equations are the continuity, momentum and scalar transport equations, respectively. d/dt is the *total* derivative and represents the time rate of change of a variable as seen by an observer riding on the moving mesh. J is a measure of the change of material volume as it travels with the moving grid. In the sliding mesh formulation, J is equal to unity, because the rotor mesh is assumed to move as solid body and hence there is no mesh distortion. Equations 3.3-7 through 3.3-9 together with constitutive relations for a Newtonian fluid are written in strong-conservation-law form in generalized coordinates.

Control volumes near the slip surface are treated differently from cells that are not bordering the slip plane. Arbitrary number of neighbors are allowed and the number of neighbors can change with time in these control volumes, made possible by introducing fictitious control volumes on both sides of the interface. Figure 3.3 illustrates this special treatment, the node P of Zone 1 are neighbored by node W, S, and E of Zone 1 and also by a fictitious node N of Zone 2.

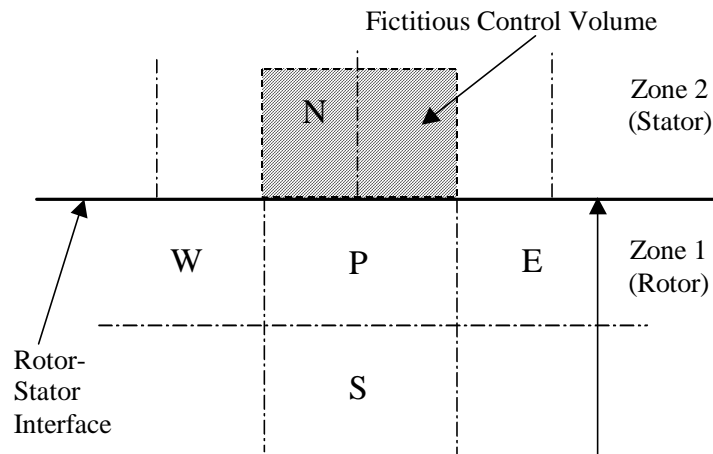


Figure 3.3 Fictitious control volume treatment of slip surface

The Sliding Mesh technique provides the best way to capture the complex internal flow where strong unsteady interactions between rotor/stator dominates the flow field. It would be the ideal tool to simulate this kind of problem if the computational cost can be reduced and compatibility with other modeling techniques enhanced. As has mentioned earlier, the Sliding Mesh model of FLUENT can not be used in conjunction with RSM model. Also, it can not be used with most of the multiple-phase models either.

3.4 EULERIAN MULTIPHASE MODEL

The primary multiple-phase model of FLUENT code is the Eulerian Multiphase model. It is derived from the single-phase model by introducing the volume fraction and a mechanism for the exchange of momentum between phases. The fundamental conservation equations are modified and applied to each phase.

The description of multiphase flow as interpenetrating continua incorporates the concept of volume fraction, denoted here by α_q . Volume fractions represent the space occupied by each phase, thus the volume of phase q , V_q , can be defined by

$$V_q = \int_V \alpha_q dV \quad 3.4-1$$

where

$$\sum_{q=1}^n \alpha_q = 1 \quad 3.4-2$$

The effective density of the phase q is

$$\hat{\rho}_q = \alpha_q \rho_q \quad 3.4-3$$

where ρ_q is the physical density of phase q , which can obey local gas law in the case of a gas.

For the fluid-fluid multiphase flow, the conservation of momentum for a fluid phase q is

$$\frac{\partial}{\partial t} (\alpha_q \rho_q \bar{u}_q) + \nabla \cdot (\alpha_q \rho_q \bar{u}_q \otimes \bar{u}_q) = -\alpha_q \nabla p + \nabla \cdot \overline{\overline{\tau}}_q + \alpha_q \rho_q \bar{g} + \sum_{p=1}^n (K_{pq} (\bar{u}_p - \bar{u}_q) + \dot{m}_{pq} \bar{u}_{pq}) + \bar{F}_q \quad 3.4-4$$

Here \bar{g} is the acceleration due to gravity, \bar{F}_q represents additional momentum sources, and \dot{m}_{pq} characterizes the mass transfer from the p^{th} to q^{th} phase. The stress-strain tensor $\overline{\overline{\tau}}_q$ in component form is given by

$$\tau_{q,ij} = \alpha_q \mu_q \left(\frac{\partial u_{q,i}}{\partial x_j} + \frac{\partial u_{q,j}}{\partial x_i} \right) - \frac{2}{3} \alpha_q \mu_q \delta_{ij} \frac{\partial u_{q,l}}{\partial x_l} \quad 3.4-5$$

The volume fraction of each phase is calculated from a continuity equation:

$$\frac{\partial}{\partial t} (\alpha_q r_q) + \nabla \cdot (\alpha_q r_q \bar{u}_q) = \frac{1}{\rho_{q,\text{ref}}} \sum_{p=1}^n \dot{m}_{pq} \quad 3.4-6$$

where $r_q = \rho_q / \rho_{q,\text{ref}}$ and $\rho_{q,\text{ref}}$ is a constant reference density. By letting the q^{th} phase be the primary liquid phase and p^{th} phase be the secondary vapor phase, one can calculate the mass transfer rate \dot{m}_{pq} in a two-phase flow due to cavitation from:

$$\dot{m}_{pq} = \frac{3\rho_p \alpha_p}{r_p} \sqrt{\frac{2(p_v - p)}{3\rho_q}} \quad 3.4-7$$

where p_v is the pressure of vaporization and r_p is the droplet or bubble radius of the secondary phase p . Volume fractions of all secondary phases are calculated, and then the volume fraction of the primary phase is obtained based on the restraint that the sum of volume fractions must be unity.

Momentum exchanges between phases in Equation 3.4-4 is based on the value of K_{pq} , the exchange coefficient. Secondary phases are assumed to form bubbles or droplets

in fluid-fluid flows, thus the predominant fluid should be modeled as the primary phase because the sparser fluid is more likely to form droplets or bubbles. The exchange coefficient of these types of mixtures is [27]:

$$K_{pq} = \frac{3}{4} C_D \frac{\alpha_p \rho_q |\vec{u}_p - \vec{u}_q|}{d_p} \quad 3.4-8$$

where ρ_q is the density of the primary phase q , d_p is the droplet diameter of the secondary phase p , $|\vec{u}_p - \vec{u}_q|$ is the relative phase velocity, and C_D is a drag function based on the relative Reynolds number. The relative Reynolds number for the primary phase q and secondary phase p can be calculated from

$$\text{Re} = \frac{\rho_q |\vec{u}_p - \vec{u}_q| d_p}{\mu_q} \quad 3.4-9$$

Then, the drag coefficient can be obtained from

$$C_D = \frac{24}{\text{Re}} (1 + 0.15 \text{Re}^{0.687}) \quad 3.4-10$$

for $\text{Re} \leq 1000$ and $C_D = 0.44$ otherwise.

The exchange coefficient for secondary phases p and r is assumed to be symmetric in the form of

$$K_{rp} = \frac{3}{4} C_D \frac{\rho_{rp} |\vec{u}_r - \vec{u}_p|}{d_{rp}} \quad 3.4-11$$

where $\rho_{rp} = \alpha_p \rho_p + \alpha_r \rho_r$ is the mixture density, $d_{rp} = \frac{1}{2}(d_r + d_p)$ is the averaged particle diameter, and $|\vec{u}_p - \vec{u}_r|$ is the relative velocity.

Equation 3.4-9 is used to find the drag coefficient except using a relative Reynolds number based on

$$\text{Re} = \frac{\rho_{rp} |\bar{u}_r - \bar{u}_p| d_{rp}}{\mu_{rp}} \quad 3.4-12$$

where $\mu_{rp} = \alpha_p \mu_p + \alpha_r \mu_r$ is the mixture viscosity.

These exchange coefficients are suited for flows with a dominant primary fluid and secondary phases forming droplets or bubbles. This makes the Eulerian Multiphase model inadequate to simulate a mixture flow with two or more major fluids, but suitable in studying flow field that may have some slight cavitation. Also, another insufficiency of the Eulerian Multiphase model is that it can not be used in conjunction with any turbulence model other than the standard $k-\varepsilon$ model or the Sliding Mesh Technique. Since the objective of the study is to investigate suspected cavitation, this model is acceptable for this portion of the research.

4.0 Simulation Setup

4.1 PRELIMINARY STUDY

Based on the conclusion and recommendations from Brothel's [1] work, the RSM turbulence model was introduced into his case setup, i.e. the same geometry and grid file, and preliminary calculation was performed, but the calculation failed to converge. The residual convergence curve, which represents how well the set of algebraic equations has been balanced, oscillated violently after a few iterations and eventually led to the divergence of the calculation. This problem also occurred in Brothel's work but in a moderate degree that an adequate but less desirable convergence criterion, 10^{-4} instead of 10^{-6} , could still be achieved. He suspected the possible reasons behind this phenomenon were the inadequacy of the turbulence model, the suspected cavitation within the energy absorber, and that the quality of the mesh, both in the total number of cells and local cell density to capture high gradient, were not high enough.

Apparently, since the RSM turbulence model itself is more prone to stability and convergence difficulties than the standard $k-\varepsilon$ turbulence model, employing it aggravated the problem instead of reducing it. Furthermore, hardware limitations, especially the size of the memory, prevented any refinement of the mesh and the calculation time had increased to an unacceptable level due to incorporating the RSM turbulence model. It was decided that an alternative approach must be used to decrease the computational labor, so that different modeling techniques can be incorporated to more accurately capture the internal flow. In order to achieve this criterion, a structured grid was employed to represent the geometry instead of unstructured grid.

In general, an unstructured grid is easier to generate in a complicated geometry because only the boundaries of the flow field need to be defined, but its triangular (2D) and tetrahedral (3D) elements require more memory to store the connectivity information of each element. On the other hand, a structured grid needs careful consideration when

applied to complex geometry such as the energy absorber because proper alignment of grid points is required. In the finite-volume approach of the CFD, the grid points, or the “nodes”, define the boundary of a small control volume, or a “cell”, to be approximate. The alignment of nodes enables a mathematical transformation of the relative node positions to generalized Cartesian coordinates and dramatically decreases the memory requirement. Also, it is relatively easy to create a locally refined grid without increasing the total number of nodes with structured grid by changing the distribution of nodes in desired area, while computer aid is necessary with an unstructured mesh.

However, it must be noted that despite the theoretical advantages of structured grids, properly generating a representation of complex geometry with it can be challenging. Certain sacrifices in representing intricate geometrical features may be necessary, and whether these approximations are appropriate must be examined. In this research, the limitation of computer resources and the fact that CFD simulation of the energy absorber is still at its early stage of development dominates the selection of a structured grid to investigate the best modeling approach.

4.2 STRUCTURED GRID GENERATION

The results obtained from any CFD code are highly dependent on the previously created grid. A “good” grid should contain as many cells as possible that are similar to the “optimum cell” and in proper node distribution. An optimum cell is a cell that best represents the cell center with algebraic averaging of the boundaries, i.e. a cell that the distances between the cell center and each cell boundary are equal, such as a square cell in two-dimensional structured grid. Node density should be increased wherever the geometry has highly curved boundaries or in the regions where the gradients of the main variables are expected to be high (boundary layers, trailing edges, etc.). Thus, the creation of the grid requires detailed examination of the problem and is often an iterative process that is controlled only by the convergence of the calculations. If the convergence is not proceeding as expected, one must refine the grid.

4.2.1 Geometry Considerations

As described earlier in the introduction, the geometry of the energy absorber consists of a double-sided rotor with eight straight radial blades and similar stators with nine straight radial blades, both within the same casing. The difference in blade numbers between rotor and stator makes it difficult to represent the geometry with a cyclically periodical calculation domain. It is assumed that due to the symmetry of the device, only half of the energy absorber will be considered in the simulation. Furthermore, the shape of the blade in computational domain needs to be adjusted to ensure proper alignment of nodes for structured grid.

Due to the fact that cylindrical geometry is very common in rotor/stator interaction problems, the FLUENT code uses a cylindrical coordinate system when performing calculation for this kind of geometry. This requires the structured grid to be comprised of straight radial lines and concentric circles, and the constant thickness blades of the energy absorber have to be approximated. It is decided that a wedge-shaped blade with one-degree angle in thickness can provide an adequate approximation to the constant thickness blade based on the dimensions of blade. Figure 4.1 shows the comparison of actual blade and computational blade.

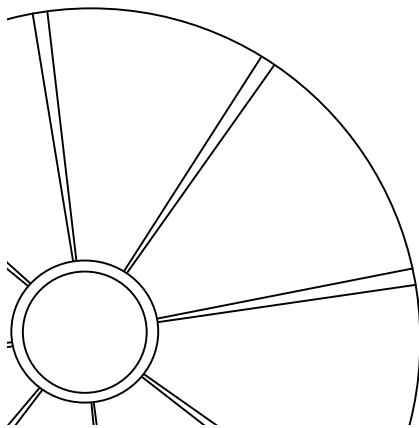


Figure 4.1a
Computational blade shape

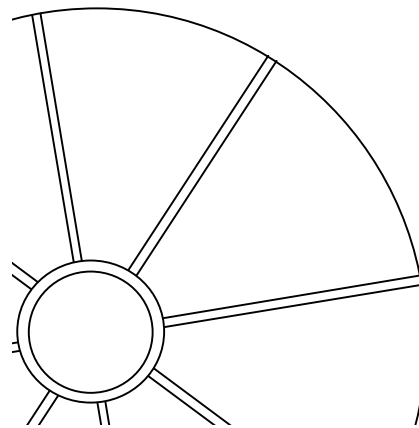


Figure 4.1b
Actual blade shape

Also, the “dead zone” between the stator and casing is neglected. This dead zone is caused by the design of the energy absorber. In fact, the actual stator geometry fits into the casing and includes the bearing that guides the rotor. Therefore a dead volume is created and the fluid can go in that region. The influence of the dead zone on the flows is weak because of its location and it is safe to neglect this region. Moreover, due to the limitation of a structured grid in a cylindrical coordinate system, the computational cells generated in this region will have too high an aspect ratio to accurately simulate the flow.

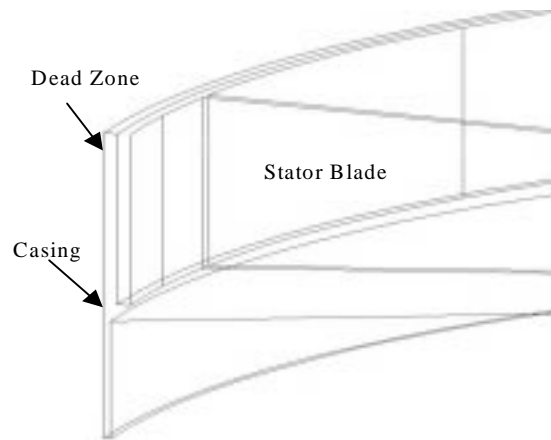


Figure 4.2 Detail of the stator and the casing geometry

4.2.2 Grid Generation

Once the necessary geometrical approximations have been made, the computational domains are defined using the P-Cube pre-processor of FLUENT. The process requires dividing the actual flow area into numerous hexahedral domains so that hexahedral cells of structured grid can be created. The work is straightforward, but highly laborious. After each domain has been created and connected to form the complete computational domain, the node distribution on the boundaries can be defined and computational cells are generated automatically based on these nodes. Figure 4.3 illustrates the building of computational domains and cells.

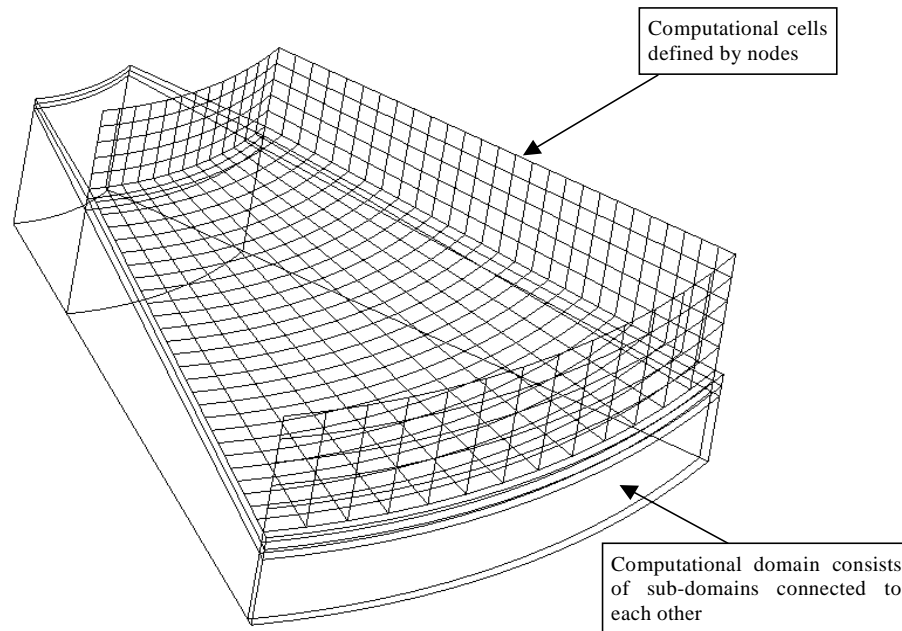


Figure 4.3 Computational domain building

The optimal hexahedral cell for CFD simulation is, of course, an exact cube. However, it is inevitable in a cylindrical coordinate system for cells with extreme radii, such as the radii in locations near the rotational axis, to have higher aspect ratio in order to obtain optimal cells in mid radius. The impact of a cylindrical coordinate system on the aspect ratio of cells is shown in Figure 4.4.

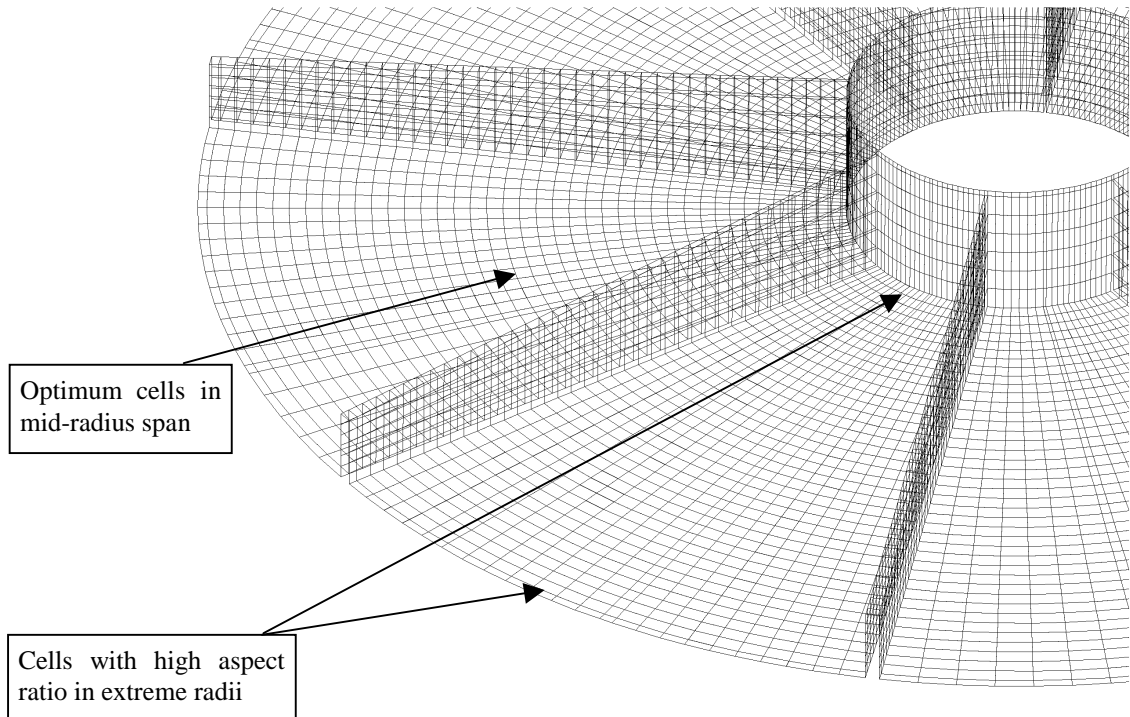


Figure 4.4 Computational cell aspect ratio variation along radial direction

The first step to generate nodes in computational domains is to decide the number of nodes in circumferential direction. Because the boundary in the circumferential direction is the longest, the highest number of nodes must be set in this direction to maintain a proper aspect ratio of each cell and thus makes it the major factor in determining the total number of cells. Due to hardware limitation, a cell with two-degree circumferential angle was chosen and the optimum cell size is calculated from its arc length at the mid-radius. Then the nodes are distributed in the axial and radial directions based on the optimum cell size and the complete structured grid is generated by the program. Figure 4.5 and 4.6 show the structured grid on the rotor and stator surfaces, respectively. Additional views of the grid are shown in Appendix A.

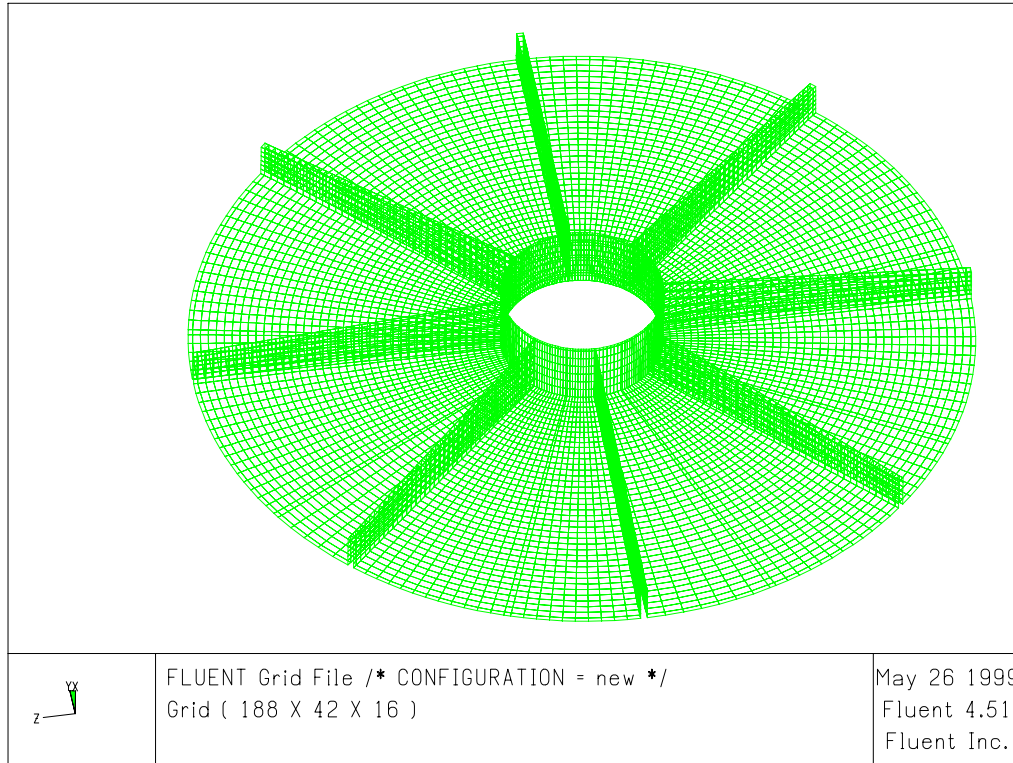


Figure 4.5 Rotor surface grid

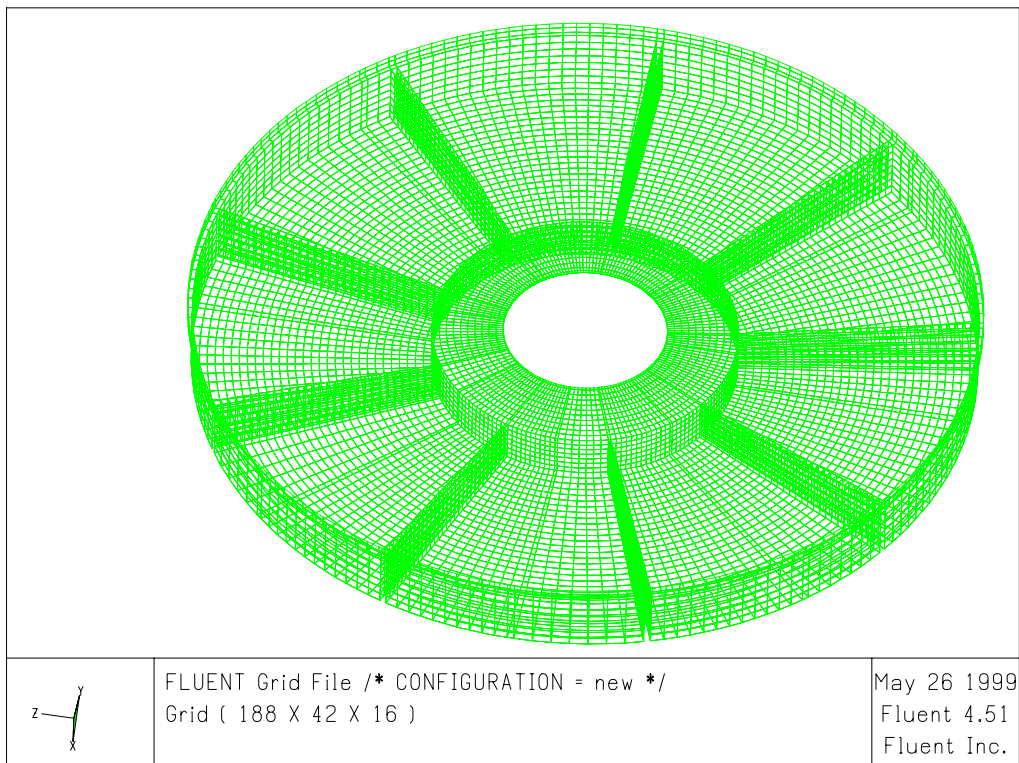


Figure 4.6 Stator surface grid

As mentioned earlier, the convergence of the calculation strongly influences the creation of the grid. The calculations performed with this grid have all reached desired convergence criteria, the residual values were less than 10^{-6} , and this shows that this particular grid provides adequate approximation of the geometry and further refinement of the grid is not required to improve the convergence. However, another grid with one-degree angle in circumferential direction and higher total number of nodes was created later on when more memory became available. The primary purpose of this finer grid is to test if the high gradients of variables in circumferential direction, especially near the blades, have been captured fully. The detail of this refined grid is included in Appendix B.

4.3 MODELING ASSUMPTIONS AND PARAMETERS

Once the grid has been created in the P-Cube pre-processor, the grid file is converted to a FLUENT case file and the next step is to set up boundary conditions before actual calculations can take place. Three different cases have been chosen to investigate the impact of different techniques in modeling the energy absorber, but some assumptions are common due to hardware limitation.

4.3.1 Basic Hypothesis

In order to decrease the time required for the calculations and to simplify the problem, one has to identify the symmetries that are present in the geometry that is to be studied. As mentioned in the previous section, only half of the energy absorber is modeled. Due to the presence of different bearings at the top and bottom of the shaft that bears the rotor, the actual geometry of the energy absorber is not exactly symmetrical. However, it is very similar, and in fact the stator blade shapes at the top of the casing are the same as the bottom ones. As a result, one can safely make the assumption that the symmetry plane of the rotor can be taken as a symmetry plane of the whole device.

The working fluid in the energy absorber is a mixture of water and anti-freeze ethylene glycol. The proportion of these two components was obtained at a late stage of the research and was tested only in comparison with one case. The working fluid in all three cases is assumed to be pure water and *the fluid has been considered to be incompressible*.

As mentioned in the literature review, the nature of the flow inside the energy absorber is such that one cannot make the simple assumption of a laminar flow. Therefore, *the flow will be considered to be turbulent*. Different turbulence models were investigated and are described in the individual case setups.

Even though thermal effects should be present within the actual energy absorber because of the frictional heat between the fluid and the rotating blades, there is no external source that transfers heat into the system. Therefore, *no heat transfer has been considered*.

Finally, although the Sliding Mesh Technique is highly recommended, it is not preferred in this research because of its incompatibility with other desired modeling techniques. The Multiple Reference Frames (MRF) technique is used to simulate the rotating flow, with some Sliding Mesh Technique tests if applicable. Different assumptions for each case are discussed individually in the following sections.

4.3.1.1 Cavitation Simulation

The unrealistically low values of the local static pressure in Brothel's work led to the suspicion of possible cavitation in the flow field and the divergence of the preliminary calculation also indicated the inadequacy of the model. As a result, a steady multi-phase calculation was chosen as the first part of this study because it required less computational effort than unsteady calculation. The simulation involved the two-phase model where the working fluids are water and water vapor, and the standard $k-\epsilon$ turbulence model was used.

4.3.1.2 Unsteady k - ε Calculation

The highly unsteady flow field within the energy absorber may not be adequately represented by steady calculation, and unsteady calculations were performed once it was found that the time dependent simulation was achievable with the available resources. The calculations were all done with the standard k - ε turbulence model and with the assumption that no cavitation occurs. Two additional calculations were also performed using this configuration, one utilizing the grid with a higher resolution in the circumferential direction, the other replacing the water with a water-glycol mixture more representative of the actual working fluid.

4.3.1.3 Unsteady Reynolds Stress Model Calculation

The integration of the RSM turbulence model into the steady calculation had been tested in a preliminary calculation, and failed to converge. The goal of introducing a time dependent simulation led to the attempt to incorporate RSM into the unsteady calculation, even though it was computational demanding. The calculation was time dependent and used the RSM turbulence model. The working fluid was assumed to be water only to avoid the cost of using the multi-phase model.

4.3.2 Modeling Parameters

The modeling parameters of the simulation are as follow:

- The MRF technique involves two reference frames, the stationary reference frame attached to the stator and the rotating reference frame attached to the rotor. Four rotational speeds have been chosen: 200, 400, 600 and 800 rpm.

- The default parameters of the software have been chosen for the working fluid:
 - Density 998.2 [kg/m³]
 - Temperature 288 [° K]
 - Pressure 101325 [Pa]
 - Dynamic viscosity 0.001003 [kg/m-s]
 - Specific heat at constant pressure 4182 [J/kg-K]
- Concerning the turbulence model, the constants that are present in both the transport equations for k and ε have been set to the default values of the software for k - ε model, while in the RSM model the default method is selected to allow FLUENT to generate boundary conditions at the wall.

Once the boundary conditions have been set, the flow field must be initialized before the iteration starts. From those initialized values, the software can calculate the new flow field and iterate until the convergence criteria are reached. This “initial guess” is very important because if the initial values are not set correctly, a converged solution may not be achieved. Thus, the data from steady calculations or a previous unsteady calculation are imported as initial values whenever possible to speed up the convergence of the unsteady simulation.

5.0 Results and Discussions

5.1 INTRODUCTION

The previous work done by Brothel [1] successfully simulates the rotating flows within the energy absorber; characteristics such as viscous behavior and secondary flow are captured. However, unrealistically low values of the static pressure give rise to the issue of possible cavitation within the flows, and the predicted torque is well below experimental values. Therefore, the primary focus of this research is to investigate the impact of sophisticated techniques in order to increase the fidelity of numerical simulations, especially in the improvement of the calculated torque, which is the major factor in the performance analysis of the energy absorber.

As described earlier, three different cases have been defined, featuring a cavitation model, unsteady calculation, and RSM turbulence model, respectively. Also, four different rotational speeds have been chosen to represent the operating conditions: 200, 400, 600, and 800 rpm. With better representation of the flow field, CFD can be used to simulate and predict desired modifications to the design.

In section 5.2, the results of two-phase simulations to investigate the suspected cavitation are treated, with corresponding figures in Appendix C. The results of the unsteady calculations with the standard $k-\varepsilon$ turbulence model are discussed in section 5.3 with accompanying figures in Appendix D. Section 5.4 treats the results of the unsteady calculation with the RSM turbulence model; the figures are shown in Appendix E. Detailed comparisons of the calculated torque for each case as well as comparison with experimental data are discussed in Section 5.5; Section 5.6 treats similar comparisons for the pressure data.

5.2 CAVITATION SIMULATION

5.2.1 Overview

The results of Brothel's work [1] showed unrealistically low values of the static pressure in cases with rotational speed higher than 200 rpm. These values were below the vapor pressure, including some regions with negative values, and were physically unrealistic. Due to the fact that the fluid had been assumed to have only one phase, it was suspected that cavitation occurred in the energy absorber and the assumption of one-phase fluid was improper. Since the numerical model that had been set did not consider the cavitation, regions that had pressure lower than the vapor pressure could not be corrected during the calculation, and eventually led to regions with negative absolute pressure.

This case setup is designed to test the cavitation model and its influence. The results show that after implementing the cavitation model, the unrealistic pressure regions occur only in 600 and 800 rpm calculations, an improvement over Brothel's results where unrealistic pressure regions could be found in 400, 600, and 800 rpm calculations. However, since incorporating cavitation model does not eliminate the problem, other inadequacies must be present in the modeling.

The standard k - ε turbulence model is used in both this case and Brothel's work. As discussed in Chapter 3 it is not particularly suited to simulate the complex flows within the energy absorber. This inadequacy of the numerical model could produce incorrect representation of the pressure distribution and eventually lead to regions with unrealistic pressures. To better understand the influence of implementing the cavitation model, graphical results of the 600 rpm case, which contains regions of both water vapor and unrealistic pressure, are discussed in the next section.

5.2.2 Graphical Results

Because the experimental pressure data are all gauge pressures, the pressures in the graphical results are presented in gauge pressure as well for easy comparison. Therefore, negative values of pressure are present and allowable in these contours. Because the absolute vapor pressure is 2338 Pa, cavitation will occur in regions with gauge pressures of -98987 Pa. Gauge pressures lower than the vapor pressure indicate regions of pure vapor, i.e. volume fraction of vapor is one and volume fraction of water is zero. Gauge pressure values lower than -101325 are physically meaningless.

The contours of static pressure on the rotor and stator at 600 rpm are shown in Figures C.1 and C.2. Although each channel of both the rotor and the stator are periodically symmetric, the static pressure distribution in each channel is not symmetric. This is due to the relative position of the rotor compared with the fixed position of the stator. For this reason, one can see higher pressure on the pressure side of some rotor blades than others. On the rotor disc segment in each corresponding channel, the static pressures are also higher than the other channels and is due to the nature of the flow in those channels which also depends on the relative position of the rotor with the stator. The relative position of the rotor with the stator can be better visualized in Figure C.7 discussed below.

Figures C.3 and C.4 represent the contours of the volume fraction of water vapor on the rotor and stator at 600 rpm. The regions with higher volume fraction of vapor correspond to the regions with low pressure in Figures C.1 and C.2 as expected, and the volume fraction shows that generally 10%-20% of these regions is taken up by gas phase. This would tend to indicate strong cavitation, but the presence of negative absolute pressure means that other numerical model issues are involved and the degree of cavitation is still in question.

Figures C.5, C.6, and C.7 represent the contours of static pressure on cylindrical surfaces concentric with the axis of rotation. The radius of those cylinders is equal to 25, 50, and 75% of the rotor blade length. The magnitude of the static pressure on the pressure side of the blade is once again dependent of the relative position of the rotor and stator blades. Pressure profiles similar to recirculating zones are also observed, such as the left foreground region of each figure, and are confirmed in Figures C.8-C.10. One can also see the exact relative position of the rotor and the stator in Figure C.7. The static pressure build-up caused by the variation of the relative position can be found in the background left region. The space between the rotor and the stator blade in the region is the smallest and presents a “bottle-neck” for the flow to pass through. The result is that the pressures are higher before this region and lower after the flow passes this obstacle.

Velocity vectors defined on the same cylindrical surfaces as Figures C.5-C.7 are shown in Figures C.8, C.9, and C.10. The velocities in the rotor passages are the highest due to the fact that the rotor is rotating and has direct influence on the fluid. Also, circumferential velocities increase as the radius increases, and the velocities in the rotor passages in Figure C.10 have the highest magnitude. Due to the no-slip condition on the rotor disc, the maximum speed above the boundary layer on the rotor disc is very close to the circumferential component $v_{\theta} = r \omega$.

Potential theory indicates that the velocity of a given flow increases locally when it has to pass over an obstacle. These increased velocities can be noticed in both the rotor and stator pressure sides (increasing velocity) and suction sides (decreasing velocities). Due to the viscous forces, the pressure gradient of the potential flow can not maintain stability and the resulting turbulence are created. In fact, once a given flow becomes unstable, the pathlines of it can not reattach to the main flow and a low-pressure zone is produced where the flow detaches. The consequence is that several secondary flow patterns are created in the flow field. Due to the highly turbulent character of the flow inside the energy absorber, detached flow or recirculating flow patterns can be found. The differences between those patterns are due to the relative position of the rotor and the stator blades.

Comparing the results with Brothel's work, it appears that employing a cavitation model does not have a noticeable influence on the velocity field, velocity magnitudes or flow patterns are very similar to his results. Figure C.11 shows the velocity vectors on the same plane defined in Figure C.9 and one can clearly see the resemblance of the two figures. The major influence of cavitation model is on the pressure values. While it again did not change the general pressure distribution much, the entire pressure field is "shifted" from the unrealistically low pressure. Figure C.12 shows the contours of static pressure on the rotor at 600 rpm of Brothel's work. Compared with Figure C.1, one can easily observe the shifting effect. A possible reason of this shifting effect could be the lack of proper boundary conditions for the k - ε turbulence model.

As discussed in Chapter 3, the standard k - ε turbulence model uses two turbulence parameters to determine all other turbulence properties. These two parameters, k and ε , are calculated from a set of differential equations that contains some empirical constants and requires certain boundary conditions. Therefore, the success of the standard k - ε turbulence model relies heavily on whether the empirical constants are appropriate to the problem and if the proper boundary conditions have been supplied. Due to the fact that no inlet and outlet exist in the geometry of the energy absorber, proper boundary conditions, such as reference k and ε values, for the standard k - ε model could not be set for this simulation. This insufficiency in the boundary conditions may lead to the "floating" of the result because there is no mathematical constraint to obtain the correct solution.

It is possible that unrealistically low values of pressure are generated because of the lack of appropriate boundary conditions and other inadequacy of the numerical model. Due to the iterative nature of CFD simulations, these unrealistic data are used in the governing equations to generate the data in the next iteration and the error is propagated during iterations. Also, without proper boundary conditions, the nature of algebraic algorithms may lower the pressure of other regions as well in order to balance the equations, and eventually lead to the entire pressure distribution being shifted. With the addition of cavitation model, extra equations are introduced into the governing

equations and provide effective boundary conditions to prevent the error from growing or such balancing.

From the comparison between Figures C.1 and C.12, one would also suspect that the calculated torque of the two cases would be very similar because the torque is calculated based on the pressure difference across the rotor blade. Since the pressure distribution does not vary much, the overall torque should remain about the same. Detailed comparisons are discussed in section 5.5 and section 5.6.

5.3 UNSTEADY k - ϵ CALCULATION

5.3.1 Overview

The inadequacy in predicting the torque in the cavitation simulation means other techniques must be implemented to improve the model. The results from the cavitation simulation and Brothel's work both show that the relative position between rotor blades and stator blades has strong influence on the pressure distribution. However, the steady state assumption means that the results only capture the flow at a certain relative position. Unsteady calculation may be necessary in order to capture the variation in the flow as the relative position changes with time.

This case is designed to investigate the influence of an unsteady calculation and a very interesting impact on the flow field is found in the results. The overall range of pressure is much larger than the steady-state calculation but the problem of unrealistic pressure is also worse. The changes in the pressure distribution indicate the dynamic effect of the flow field has been captured, but other modeling assumptions or techniques are insufficient to correctly represent the pressure. First, to save computational time, this case again assumes one-phase fluid and the influence of this assumption has been shown in the cavitation simulations. Second, advanced turbulence model such as the RSM model has not yet been implemented. Third, Multiple Reference Frames technique is used due to hardware limitation and its capability to accurately simulate the interface region between the rotor and the stator is insufficient.

5.3.2 Graphical Results

Only the results of 200 rpm calculation show no sign of any unrealistically low pressure. However, for easy comparison with other cases, the graphical results of 600 rpm calculation are discussed in this section. The results after two full revolutions of the

rotor, i.e. the initial relative position and the same relative position as steady-state calculation, are shown and the pressure values in the results are gauge pressure.

The contours of static pressure of the rotor and the stator are shown in Figures D.1 and D.2. The dramatic difference between these figures and Figure C.1-C.2 is the scale of pressure distribution. The maximum value of pressure in this case and the cavitation simulation are both at around 300 kPa, but the minimum value of this case is more than 600 kPa lower than the cavitation simulation. While these extremely low values are physically meaningless, the experience in cavitation simulation indicates that it may be because of the failure of numerical techniques rather than the analytical modeling assumptions.

The dynamic effect when the rotor blades pass the stator blades is captured. When a rotor blade passes a stator blade, the spacing for the fluid to pass is minimized and the flow has to accelerate to pass the obstacle. As the rotor blade repetitively passes the stator blades, it will create a low-pressure region on the top of the rotor blade because the flow across this region will have higher velocity. One can easily notice the appearance of such low-pressure regions at the mid-span of rotor blades in Figure D.1. Also, at the region where the hub of the stator blades exists, a corresponding high-pressure region can be found at each rotor blade. This is created when the flows that turn away from the hub of the rotor blades and the flows that can not pass the spacing between the rotor blades and the stator blades encounter at this region.

Compare the results with Figure C.1, one can find that this dynamic effect was not noticeable in steady-state calculation. This is due to the fact that steady-state calculation does not change the relative position between the rotor blades and stator blades, therefore the effect of repetitive passing of the blades can not be account for. However, the pressure distribution in each channel is not symmetric as in Figure C.1. This could be due to the fact that Multiple Reference Frames techniques still employs certain steady-state assumption to speed up the calculation and thus the initial relative position will still have influence on the following iterations.

Figure D.3, D.4, D.5 and D.6 represent the contours of static pressure on cylindrical surfaces concentric with the axis of rotation. The radii of those cylinders are equal to 25, 50, 75, and 99% of the rotor blade length. The low-pressure zones at the top of the blades caused by the passing of the blades can be easily visualized. Also, pressure profiles of secondary flows are found, such as the low pressure regions in the background left of Figures D.4 and D.5 suggest possible recirculating flows.

Figure D.7 shows the contours of static pressure on the interface plane between the rotor and the stator. At this plane, absolute values of the velocities from the two different reference frames, stationary and rotating, are matched. The low-pressure regions are located above the top of the rotor blades and the effect of the blades passing is not apparent on the regions near the top of the stator blades. This is because as the rotor blades rotate, they are continuously forcing the fluid to accelerate and flow through the corresponding stator passage, regardless of the cross-sectional area of the passage. On the other hand, the fluid in the stator region is being dragged with the fluid in the rotor region and the acceleration effect would not be at the same magnitude.

Velocity vectors defined on the same cylindrical surfaces as Figures D.3-D.5 are shown in Figures D.8, D.9, and D.10. One can see that the flow is turning away from the hub of the stator and the radial components of the velocities are outward in the foreground of Figure D.8. However, in the corresponding zone in Figure D.9 and D.10, the radial components of the velocities is either inward or near zero, indicating the flow is turning away from other obstacles or the stagnant region where flows from different direction combine. Also, recirculating secondary flows can be seen in the background left region of Figures D.9 and D.10 and correspond to the low pressure regions seen in Figures D.4 and D.5.

Figure D.11 presents the velocity vectors on the same interface plane described in Figure D.7. Secondary flows such as detached flows and recirculating flows can be found near the hub of the stator blades. One can also see the locally accelerated flow on the top

of the rotor blades. Bear in mind that the variable viewed in this figure is the absolute velocity. The rotor blades see the high velocity that is the sum of the absolute velocity and rotational speed.

While the problem of unrealistically low pressures still plagues the simulation, the dramatic change in the overall pressure profile with unsteady calculation is a sign of improvement. In fact, the comparison with the experimental torque data shows that the predicted torque is much closer to the experimental value than any result from steady-state calculations. Detailed comparisons and discussions will be provided in section 5.5 and section 5.6 after the results of the unsteady RSM calculations are discussed.

5.4 UNSTEADY REYNOLDS STRESS MODEL CALCULATION

5.4.1 Overview

As mentioned in Section 4.1, attempts to employ the RSM turbulence model into the steady-state unstructured grid calculations have been made but without success. Further calculations were performed once the structured grid was generated, but again the calculation failed to convergence. With the suspected cavitation in mind and the fact that some multiple-phases modeling is not compatible with the RSM model, further studies to implement it were postponed.

In the FLUENT manual [28], it suggests that a strategy to reach convergence is to perform an unsteady calculation and let the scheme converge to a steady-state solution instead of performing a steady-state calculation. Because the source code of the program is not available, exact reason behind is still unknown. However, some background calculations can be used to explain the possible reasoning of this strategy.

When performing unsteady calculations, the results of last iteration, or previous time step, have influence on the current iteration because of the time term in the governing equations. Therefore, a proper choice of the size of the time step is important to ensure the stability of the scheme, the convergence of the calculation, and the accuracy of the solution. This demands that any numerical scheme allow a user to define the size of the time step or change it during iterations to guarantee the success of the CFD simulation. On the other hand, when performing steady-state calculation, the time terms in the governing equations must be set to zero to reflect that the equations are time-independent and no control over the size of the time step seems necessary.

However, in a numerical sense, setting the time terms to zero can be accomplished simply by setting the size of the time step to be very large or infinite so that the change in the variables is relatively small compare to the difference between each

step and is approximately zero. In fact, it is not uncommon to use this technique in an unsteady calculation to speed up its convergence to an “averaged” steady-state solution. Such a numerically equivalent step size when setting the time terms to zero in the steady-state calculation may sometimes cause the numerical scheme to be more prone to stability and convergence problem, because proper step size to define the relations between numerical iterations can not be set. To avoid such problem, time terms must be preserved, i.e. an unsteady calculation, in the governing equations so that the step size can be controlled to stabilize the scheme.

Following the suggestion in the manual, several step sizes were tested and the results show that a step size of 0.0001 sec is necessary in the initial stage to successfully employ the RSM turbulence model. In comparison, a step size of 0.001 sec works very well through out the iterations in the unsteady calculations with the standard $k-\varepsilon$ turbulence model discussed in section 5.3.

The results of the unsteady RSM calculation have similar profiles of pressure distribution as the unsteady calculation with the standard $k-\varepsilon$ model, but the actual values of the pressure are much higher. Also, the velocity field of both cases are very similar. Graphical results in gauge pressures of the 600 rpm calculation after two full revolutions are discussed in the next section to explain this interesting similarity.

5.4.2 Graphical Results

The contours of static pressure on the rotor and the stator are shown in Figure E.1 and E.2. The overall differences in the pressure profiles between these two figures and Figures D.1 and D.2. are hard to notice. The major difference is the values of the pressure. One can easily see that in Figure E.1 the maximum and minimum values of pressure are about 547000 Pa and -449000 Pa respectively, while in Figure D.1 the same values are 142000 Pa and -791000 Pa. The same increase can also be found in Figure E.2 compared to Figure D.2. While the unrealistically low values of pressure still exist, this

indicates that introducing the RSM model does increase the fidelity of pressure data substantially.

A more interesting discovery is that switching to the RSM model from the standard k - ϵ model only changes the pressure profile slightly but shifts the values of pressure dramatically. This is very similar to the “shifting” phenomenon found in the cavitation simulation when compared to Brothel’s result. The same reasoning regarding the insufficiency in proper boundary conditions for the standard k - ϵ model can be applied as well. Because the RSM model is less dependent on the boundary conditions, the unrealistically low values of pressure can be greatly improved. However, due to the inadequacy in other modeling techniques and the fact that proper boundary conditions are still absent, these unrealistic values still appear.

Figures E.3, E.4, E.5 and E.6 represent the contours of static pressure on cylindrical surfaces, concentric with the axis of rotation, at 25, 50, 75, and 99% of the rotor blade length. The low pressure region at the top of the blades can be seen in these figures. This again demonstrates that an unsteady calculation is necessary to capture the dynamic effect, such as the passing of the blades. Pressure profiles of secondary flows are also found, such as the low pressure regions in the background left of Figure E.4 suggest possible recirculating flows.

Figure E.7 shows the contours of static pressure on the interface plane between the rotor and the stator. Again, the low-pressure regions are above the top of the rotor blades more developed and the same effect is not apparent on the regions near the top of the stator blades. As discussed previously, this is because the rotor blades are continuously forcing the fluid to flow pass them while the fluid is being dragged to pass the stator blade.

One can clearly see the pressure profiles of Figures E.3-E.7 resemble those of Figure D.3-D.7 while the upward shifting of the pressure values makes the results more convincing. Comparing these figures, one can find that the pressures in the unsteady

RSM calculation are about 400000 Pa higher than those in the unsteady $k-\varepsilon$ calculation. This is very similar to the amount observed when comparing Figures E.1 and E.2 to Figures D.1 and D.2.

Velocity vectors defined on the same cylindrical surfaces as Figures E.3-E.5 are shown in Figures E.8, E.9, and E.10, and Figure E.11 shows the velocity vectors on the same interface plane with Figure E.7. The velocity fields illustrated in these figures also show resemblance with the results in Figure D.8-D.11. In fact, they are much similar because the differences in the velocity magnitudes are only 10%, unlike the dramatic shift found in the pressure profiles. This similarity again resembles the same effect found when comparing the results of the cavitation simulation with Brothel's results.

The shifting in the values of the pressure indicates that applying the RSM model, while reducing the problem of unrealistically low pressure, may not change the calculated torque very much. A detailed comparison of the calculated torque will be discussed in the next section.

5.5 TORQUE CALCULATIONS

As previously mentioned, evaluating the torque transmitted to the shaft is essential in the design or the performance analysis of the energy absorber. Therefore, correctly predicting the torque is one of the major factors in determining the success of the CFD simulations. The torque is generated by the resultant of fluid forces applied on the rotor surface, which can be separated in two different contributions:

- The pressure contribution which is created by the pressure forces acting normally to the surface of a given body, and
- The viscous contribution which is created by the shear stresses acting tangentially to the surface of a given body

The torque calculation is accomplished by calculating the resulting force from the pressure and stress tensor distribution on a desired surface, and the moment vector about a specific axis is then computed by summing the product of the force vectors with the moment arm vector. The FLUENT code has the capability to perform this calculation automatically with user-provided moment axis and desired surfaces, and this post-processing function provides the data presented in this section.

On the other hand, the original experimental data are very “noisy”; mechanical vibrations caused by the dynamic effect of the flows are also recorded due to the limitation of the measurement instrumentation. However, from an analytical point of view, the energy absorber acts as a fluid brake in which the torque generated should be a function of the square of the rotor’s angular velocity. An analytical flow model of the energy absorber based on the fundamental fluid dynamic theory has been developed under another effort by Virginia Tech. The resulting torque model can be expressed as

$$T = K \cdot \omega^2$$

where ω is the rotational speed in rpm and K is a constant of proportionality based on

- Reynolds number in the circumferential component.

- density of the fluid.
- radius of the rotor
- radius of the tub
- height of the rotor blade

It is found that by setting $K = 0.155$ for torque in English Units (or $K = 0.210$ for torque in SI Units), the analytical model represents the experimental data extremely well. This well-developed analytical model will provide the experimental data presented in the discussion.

5.5.1 Dynamic Torque Effect

As described earlier, a suspect reason for the underestimation of the torque in steady-state calculations is that it fails to capture the change of the relative position of the blades. It is possible that only an unsteady calculation can take into account the dynamic change in the torque due to the variation of the relative position and correctly predict the torque. The dramatic change in the pressure distribution indicates that the results from the unsteady calculations should improve the predicted torque as well. Detailed comparisons and discussions in this section will provide the evidence that the unsteady calculations have captured the dynamic variation of the torque.

Figure 5.1 shows the comparison of the dynamic torque of the 600 rpm calculation between the three case setups and Brothel's result. One can clearly see the dynamic change in the torque during the unsteady calculation while the steady-state calculations have constant values of torque. With the variation of the relative position of the blades, the torque varies in time. A periodic behavior in the variation of dynamic torque can also be found, it can be explained by the fact that the change in the relative position of the blades is periodic also, with a period of one revolution.

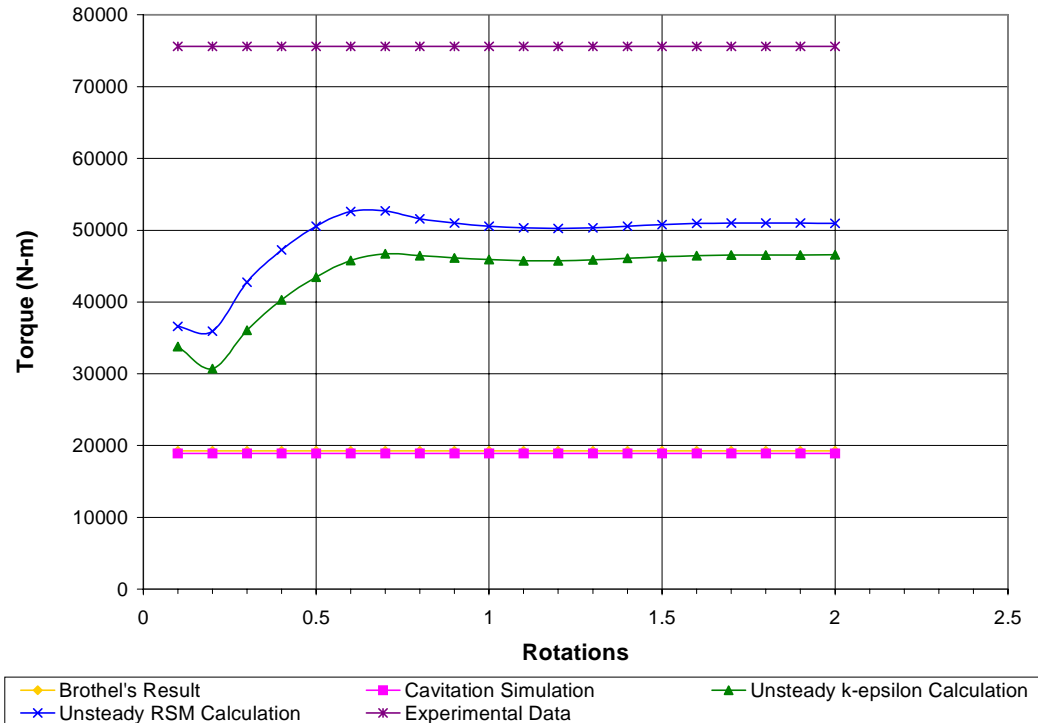


Figure 5.1 Dynamic torque comparison

Another interesting behavior is that the oscillation of the torque in the second revolution is much less than in the first revolution. In fact, the variation is small enough that one can consider the unsteady calculation has converged to a steady-state “average” solution. The possible reason for this behavior is the Multiple Reference Frames model. As discussed earlier, since the MRF model incorporates steady-state assumption in treating the interface region between reference frames, some unsteady variations in the flow field may not be accounted for and cost less computational time. Therefore, fewer time steps are required for the simulation to reach the steady-state average solution.

It can be seen that the torque data in the unsteady calculations are much higher than either steady-state calculation. In fact, the torque data of both unsteady calculations at the end of the second rotation are more than twice of that of either steady-state calculation. Because the original torque value of Brothel’s result is much lower than the experimental data, this increase is very encouraging. This improvement shows that with the unsteady calculation, dynamic effects that would increase the torque, such as the

passing of the blades, is accounted for. Table 5.1 lists the torque values of each case after two full rotations and provides a better demonstration of the substantial increase in the unsteady calculation.

Table 5.1 Comparison of torque data after two full rotations

Case Setup	Torque Value (N-m)		
	Pressure	Viscous	Total
Brothel's Result	19179	79	19258
Cavitation Simulation	18795	89	18884
Unsteady $k-\epsilon$ Calculation	45980	572	46552
Unsteady RSM Calculation	50340	590	50930
Experimental Data	n/a	n/a	75600

From Table 5.1, one can also note that the viscous torque of the unsteady calculation is extremely high compare to the steady-state calculation. This is another indication that with the simulation of dynamic effects, the flow field characteristics are much different from the results of steady-state calculation. However, the values of the viscous torque are much smaller than that of the pressure torque and the total values remain roughly the same. Also, the predicted torque of the cavitation simulation is very close to Brothel's result. As discussed in section 5.2, this is not surprising since the pressure distribution in both simulations is very similar and the only major difference is the "shifting" of the pressure values. The similar shifting of the pressure field that is observed in the unsteady RSM simulation when comparing with the results in the unsteady $k-\epsilon$ simulation could also explain the slight increase in the torque after applying the RSM model to the unsteady calculation.

5.5.2 Additional Unsteady Calculations

As mentioned in Chapter 4, additional unsteady calculations with different fluid properties and refined grid are performed. Due to the similarity of the results, graphical profiles for individual test are neglected, and only the numerical data will be discussed. The first case uses the refined grid described in section 4.2.2, which consists of computational cells of one-degree circumferential angle. This refined grid is designed to test whether the high gradient near wall has been captured. The second case uses a water-glycol mixture that is more representative of the actual working fluid within the energy absorber. The case is design to test if the calculation done with pure water is accurate enough to reflect the true working fluid. Table 5.2 lists the different physical properties used in the mixture simulation and the original case.

Table 5.2 Physical properties comparison

Fluid	Density (kg/m ³)	Viscosity (kg/m/s)
Water	998	1.003 X 10 ⁻³
Water-Glycol Mixture	1056.75	1.151 X 10 ⁻²

One can see that the increase in the fluid density is about 5%, while the viscosity of the mixture is an order of magnitude higher than pure water. As mentioned previously, based on fluid dynamics theory the torque is expected to be

$$T = K \cdot \omega^2$$

where K is linearly proportional to the fluid density and ω is independent of the viscosity and the density. Because the viscous torque is much less than the pressure torque, one would expect that the 5% increase in the density should lead to approximately 5% increase in the calculated torque. The comparison provided below validates this rationalization. Figure 5.2 shows the comparison of the torque data for the various 600-rpm unsteady calculations; the torque values after two full rotations are summarized in Table 5.3.

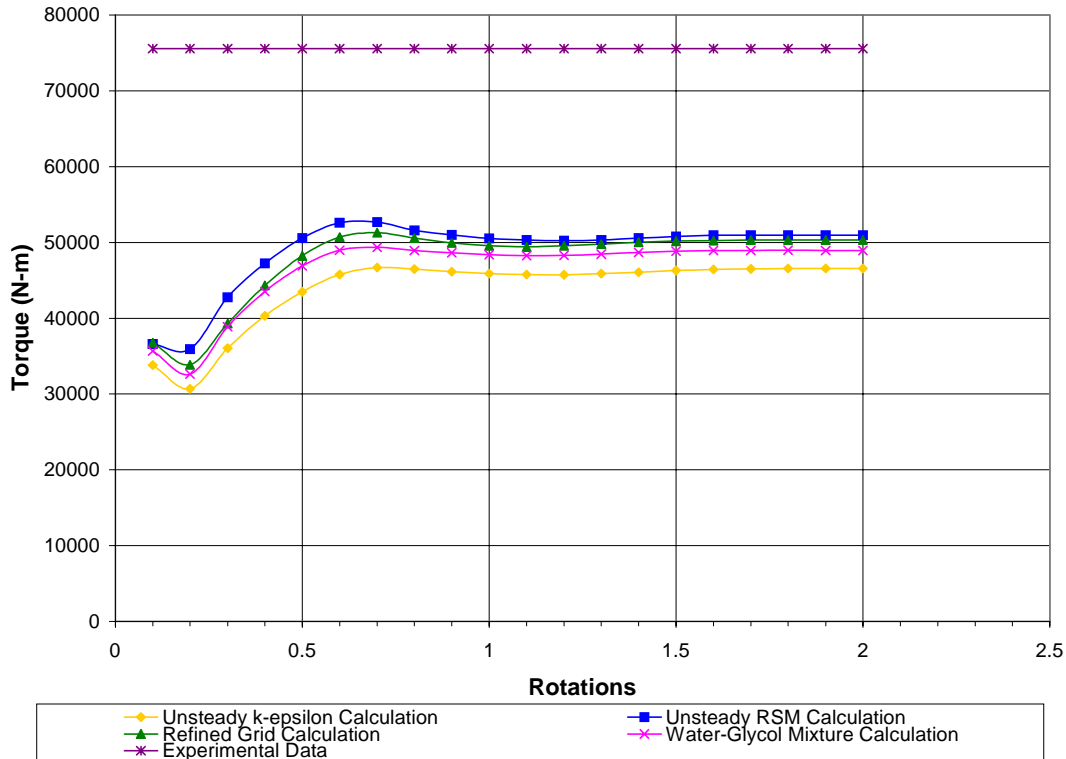


Figure 5.2 Torque comparison of the additional unsteady calculations

Table 5.3 Comparison of torque data after two full rotations

Case Setup	Torque Value (N-m)		
	Pressure	Viscous	Total
Unsteady k-ε Calculation	45980	572	46552
Water-Glycol Mixture	48680	262	48942
Refined Grid Calculation	49710	596	50306
Unsteady RSM Calculation	50340	590	50930
Experimental Data	n/a	n/a	75600

From the data, one can clearly see the result of the mixture simulation is approximately 5% higher than the original torque calculation. While this is a validation of the CFD result in this research, it also demonstrates that CFD simulation could be used to validate theoretical analysis if the analytical model has not yet been proven. Also, one would notice that the viscous torque decreases although the viscosity of the mixture is higher than pure water. It must be noted that the torque is a vector not a scalar, a possible

explanation of such phenomenon is that the viscous torque in the negative direction increases as the viscosity of the mixture increases.

Table 5.4 Comparison of viscous torque after two full rotations

Fluid	Viscous Torque (N-m)			
	200 rpm	400 rpm	600 rpm	800 rpm
Water	25	679	572	346
Water-Glycol Mixture	646	478	266	-113

Table 5.4 shows the data of the viscous torque from the two unsteady calculation cases using different working fluids. One can clearly see the decrease of the viscous torque as the viscosity or the rotational speed increases. Again, since the viscous torque is a vector, this means that the magnitude of the torque in the negative direction increases as these properties increase. However, it seems physically unrealistic to actually have lower viscous torque when the rotational speed increases. In fact, the results from steady-state calculations do not have this behavior and the viscous torque increases with the rotational speed. The fact that there are also regions with unrealistically low values of pressure suggests that this is another result of the same inadequacy in the numerical model.

Another case presented in Figure 5.2 is the calculation done with a refined grid. The improvement in the torque calculation is evident but limited, especially considering the increase in the required computational time and storage encountered in the simulation. This shows that the general resolution of the grid is fine enough, especially in the circumferential direction where the resolution was doubled. Further refinement of the grid should focus on the distribution of nodes to increase the local resolution where the gradients of the variables are high.

5.5.3 Experimental Data

With the characteristic of the predicted torque in each calculation discussed, comparison with the experimental data will be addressed in this section. One can easily notice that the pressure torque is the dominant part in the torque calculation and the change in the predicted torque depends highly on the variation in the pressure distribution from the previous discussions. However, certain problems, such as the unrealistic pressure, still plague the pressure distribution in the calculation and the accuracy in the resulting torque value is also in question.

Table 5.5 Experimental and numerical values of the torque

Speed	Experimental	Brothel's Result			Cavitation Simulation		
		Total	Pressure	Viscous	Total	Pressure	Viscous
(rpm)	(N-m)	(N-m)	(N-m)	(N-m)	(N-m)	(N-m)	(N-m)
200	8400	2093	10	2103	2257	9	2265
400	33600	8398	36	8435	9352	33	9385
600	75600	19179	79	19258	18795	89	18884
800	134400	37554	143	37697	39259	73	39332

Speed	Experimental	Unsteady k-ε Calculation			Unsteady RSM Calculation		
		Total	Pressure	Viscous	Total	Pressure	Viscous
(rpm)	(N-m)	(N-m)	(N-m)	(N-m)	(N-m)	(N-m)	(N-m)
200	8400	5564	25	5589	5696	27	5723
400	33600	22390	679	23069	24442	700	25142
600	75600	45980	572	46552	50340	590	50930
800	134400	89080	346	89426	96962	357	97319

Table 5.5 lists the torque values of each case, including Brothel's work, and the experimental torque. Figure 5.3 provides a graphical comparison of these results. All four cases have captured the characteristic of the experimental/analytical model that the torque is proportional to the square of the rotational speed. However, the predicted torque in both steady-state calculations is only about 30% of the analytical value. The results in the unsteady calculations are much better, but still at only about 70% of the experimental torque.

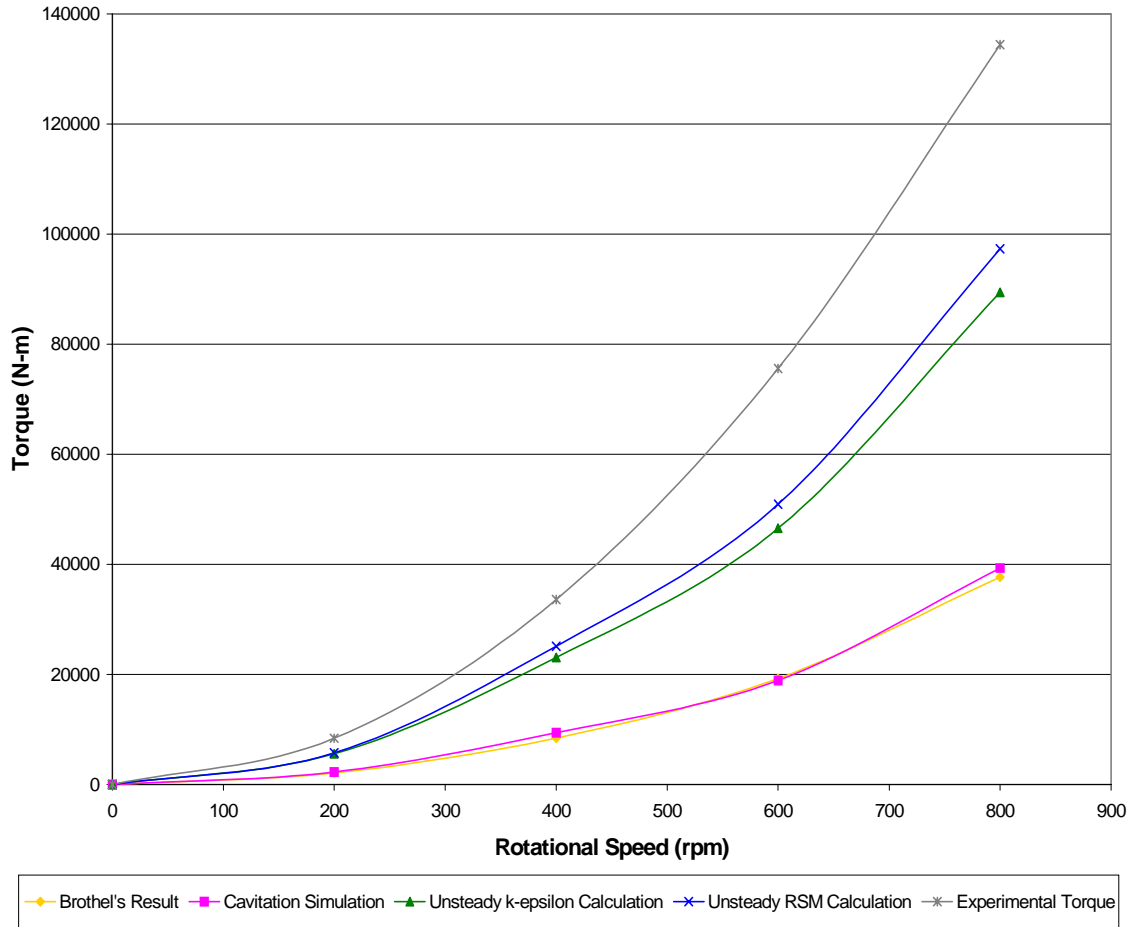


Figure 5.3 Comparison of torque values with experimental data

From the Figure 5.3 one can see that virtually no improvement in the predicted torque is achieved by introducing cavitation model, while applying the RSM model provides certain improvement in the calculated torque. The large difference between the results from the unsteady calculations and the results from the steady-state calculations shows that it is necessary to perform unsteady calculation to accurately predict the torque. Several possible explanation for the 30% torque that is unaccounted for in the CFD simulations are listed below:

- The steady-state interface assumptions of the Multiple Reference Frames model means that the calculation is not an unsteady simulation. Since the results show that the time-dependent effect in the flow field is the primary factor in correctly predicting

the torque, the MRF model appears to be inadequate. A better approach is to employ the Sliding Mesh Technique, at the cost of increased time and memory.

- While the RSM model and the cavitation model each show limited success in improving the torque calculation, the fact that unrealistically low pressure still exist in both calculation suggests that the two models should be working in conjunction to properly simulate the flows. This incorrect calculation of the pressure distribution will certainly lead to errors in the calculated torque.
- The grid may not be fine enough to capture the high gradients near the walls. As discussed in the last section, refinement in the grid does improve the torque calculation, although at a high cost. Also, because the blades are wedge-shape in the computational domain, the geometry at tip, where the highest pressures exist and has the longest moment arm, is incorrect. Both may cause minor error when predicting the torque.
- The properties of the working fluid are not accurate enough, as discussed in the last section. This can be fixed by using the mixture properties.

5.6 PRESSURE DATA ANALYSIS

Since the torque resulting from the pressure forces is the dominant component of the total calculated torque, an accurate representation of the pressure distribution is necessary to correctly predict the torque. Therefore, the fact that the predicted torque values of the CFD simulations are lower than the experimental data also indicates certain inaccuracies exist in the pressure profiles. In order to better understand the reasons behind the underestimation of the torque, experimental pressure data and the CFD pressure results are discussed in this section.

Experimental pressure data in the energy absorber is hard to obtain, since its geometry and the instantaneous nature of its operation limits the measurement methods. For example, although the pressure profile on the rotor is the desired information, it is extremely difficult to obtain such data because the sensors may fall off at higher rotational speed. Despite the high cost of acquiring experimental data, the Aircraft Division of Naval Air Warfare Center, located at Lakehurst, NJ, performed a series of experimental tests to provide information for the design of the energy absorber. Fourteen pressure transducers were placed on the bottom of one of the stator channels, i. e. the surface of the stator between two stator blades, from the hub to the tip of the stator at an increment of approximately 25% of the stator blade length. Five were placed along each blade and the other four were along the centerline of the channel. Figure 5.4 illustrates the locations of these pressure transducers.

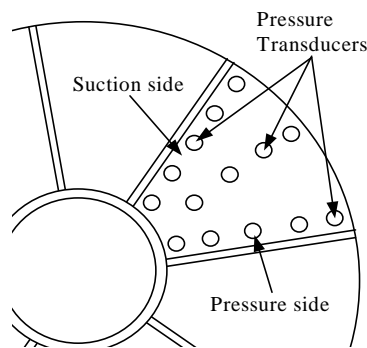


Figure 5.4 Pressure transducer locations

By measuring the surface pressure, it is inevitable that mechanical vibrations, or “ringing”, would also be recorded and this would compromise the accuracy of the pressure data. Also, it is difficult to correctly filter the data, because the extreme data values may be the points with moderate pressure but subject to excessive mechanical fluctuation or vice versa. For this reason, while the experimental torque data have been analyzed and a well-developed analytical model provides the data discussed thus far, experimental pressure data have not yet been refined or analyzed to such an extent. The experimental data presented in this section are very “noisy” and some unrealistic pressures are reported.

Figure 5.5 and 5.6 show the comparison of the pressure on the pressure and suction sides of the stator channel at 50% of the stator blade length, respectively. Because the CFD simulations are all done at a certain rotational speed, pressure data from the same relative position in all nine stator channels are plotted to represent the pressure variation when the relative position between rotor and stator changes as different rotor blades passing one stator channel. In Figure 5.5, the second-order polynomial trendline of the experimental data passes through the upper range of pressure data of the cavitation simulations and the unsteady RSM calculations, while the data for the unsteady $k-\epsilon$ calculations are lower and unrealistic. One can also see some of the experimental data are unrealistic, this is due to the influence of mechanical vibrations discussed earlier. On the other hand, the trendline in the Figure 5.6 is slightly higher than the pressure data predicted by either cavitation simulations or unsteady RSM calculations, while the data of the unsteady calculations remain low and unrealistic.

The results show that both cavitation simulation and unsteady RSM calculation have captured the pressure values in these regions adequately well, with some slight underestimation. However, the unsteady $k-\epsilon$ calculation provides poor representation of the actual pressure. As discussed previously, the standard $k-\epsilon$ model is insufficient to capture the flows within the energy absorber because proper boundary conditions can not be set and may be responsible for the problem of unrealistic pressure. The results presented here again prove that introducing the cavitation simulation or the RSM model

reduce the problem. In fact, the shifting of the pressure values when employing the RSM model discussed previously can be found in these figures as well. For example, the range of pressure data of 600 rpm in the unsteady $k-\epsilon$ calculation is about 80 psi lower than that in the unsteady RSM calculation in both figures.

Since the predicted pressure in these regions are close to the experimental values, the calculated torque should be close to experimental torque as well. In fact, the calculated torque may be higher than the actual value because the pressure on the suction side is underestimated more. However, as discussed previously all calculations predicted a lower torque than the experimental result, this indicates that the pressure in the other regions is not correctly captured.

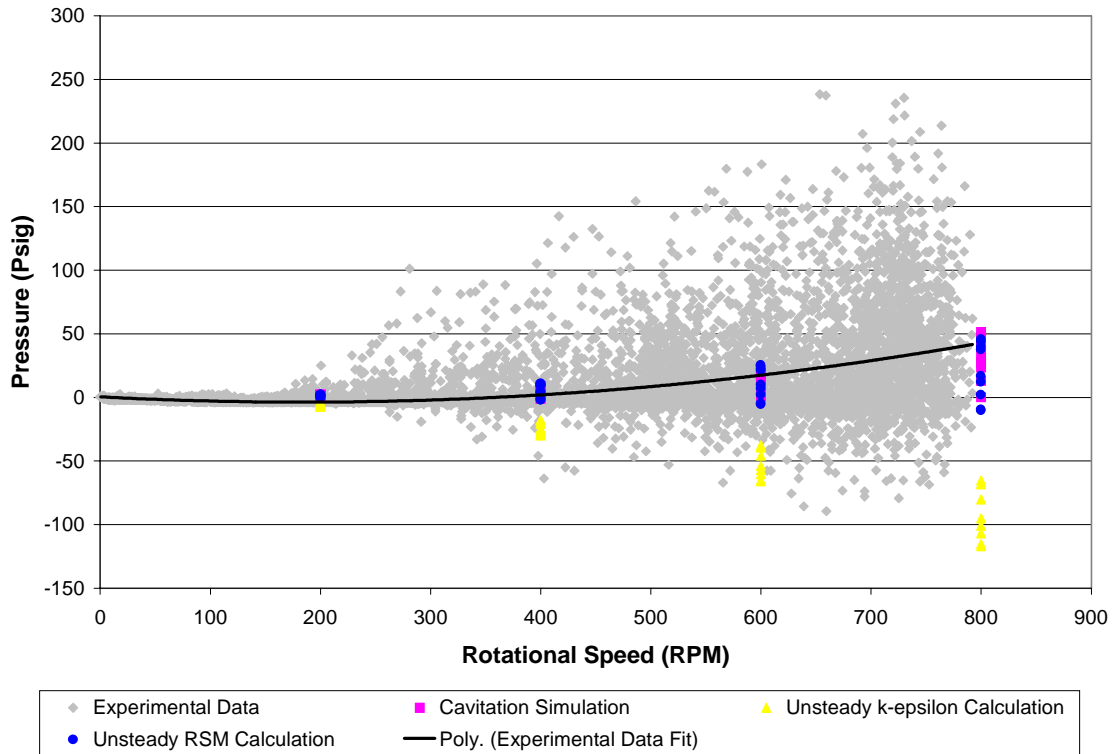


Figure 5.5 Pressure data comparison: pressure side, 50% of stator blade length

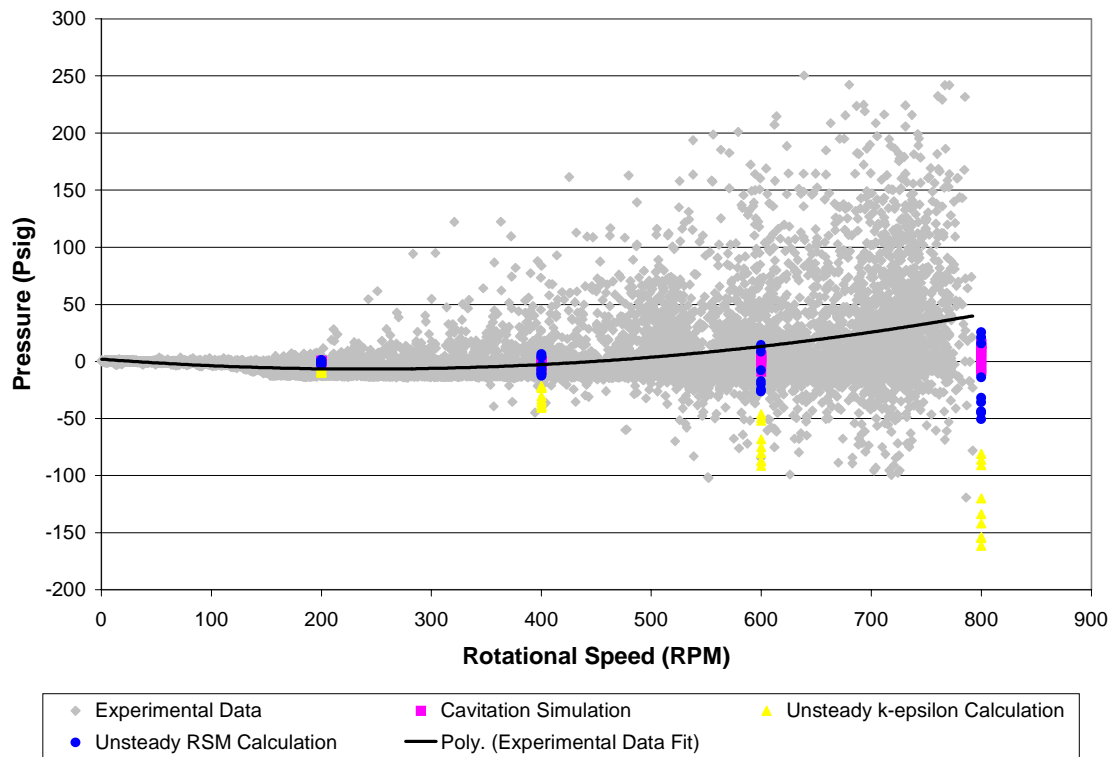


Figure 5.6 Pressure data comparison: suction side, 50% of stator blade length

Figures 5.7 and 5.8 provide similar pressure comparison with Figure 5.5 and 5.6 at the hub of stator. The results, however, are not very similar. Underestimation of the pressure in both stations is evident, with the unsteady RSM calculation provides slightly better approximation than the other two cases. In fact, the results of the unsteady RSM calculation cover a wider range and the points in the lower range are not as good.

The results indicate that the flows in the hub region are not captured fully. Due to the fact that the regions in the figures are at the corners of the stator blade channel, pressure in these regions are expected to be higher than in regions near the mid-span of the blade. The amount of turning required for the flows to overcome the obstacle is greater and therefore the pressure force exerted on the blade is also greater. Also, a corner may become a stagnation point that the flow loses its momentum when it can not overcome the obstacle. The underestimation of the pressure implies that the momentum equations, which relate the pressure and the turning of the flows, are not solved correctly. From the graphical results discussed previously, the simulated flow field near this region varies when switching from a steady-state calculation to an unsteady calculation. A possible explanation of the underestimation of pressure is that certain dynamic effects have not yet been captured fully by the calculation employing the Multiple References Frames technique and the pressure was not capture correctly.

Although the pressure has not been calculated correctly, one can notice that the underestimation in both figures is approximately the same. For example, the experimental trendline value at 600 rpm is about 70 psig in both figures, and the mid-point value of the pressure range of the unsteady RSM calculation is about 25 psig in both figures also, with the value in the suction side slightly lower than in the pressure side. Therefore, when calculating the torque, the difference in the pressure values would be cancelled out and the predicted torque should remain accurate. This indicates that the torque calculated in these regions might not contribute to the error in the predicted torque and other regions must be studied. Due to the similarity in geometry of the tip region and the hub region, one would suspect underestimation of pressure also occurs in the tip region. The comparisons of pressure data in the tip region are shown in Figure 5.9 and 5.10.

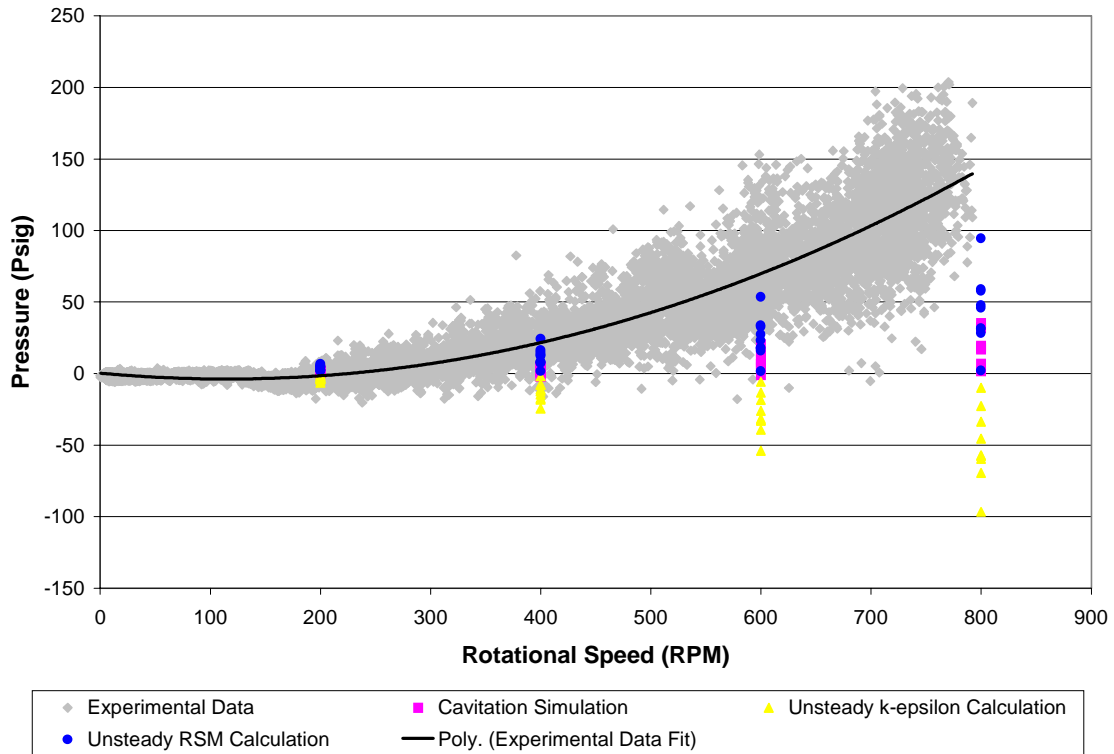


Figure 5.7 Pressure data comparison: pressure side, hub of stator blade

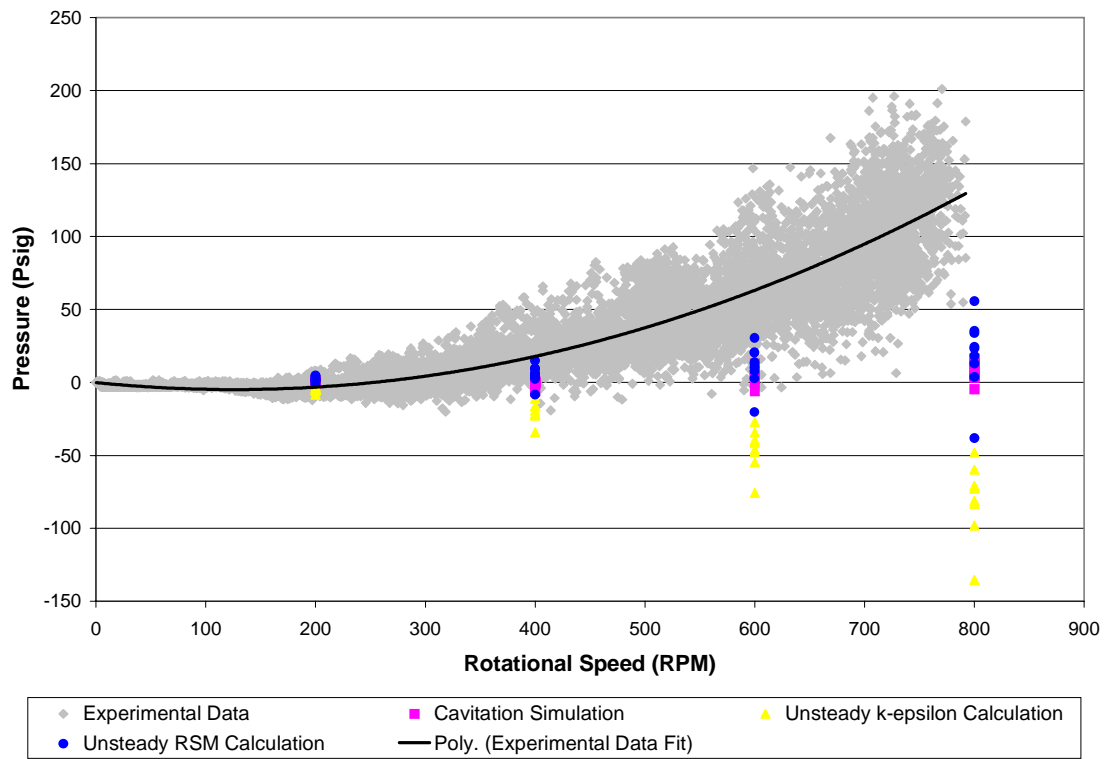


Figure 5.8 Pressure data comparison: suction side, hub of stator blade

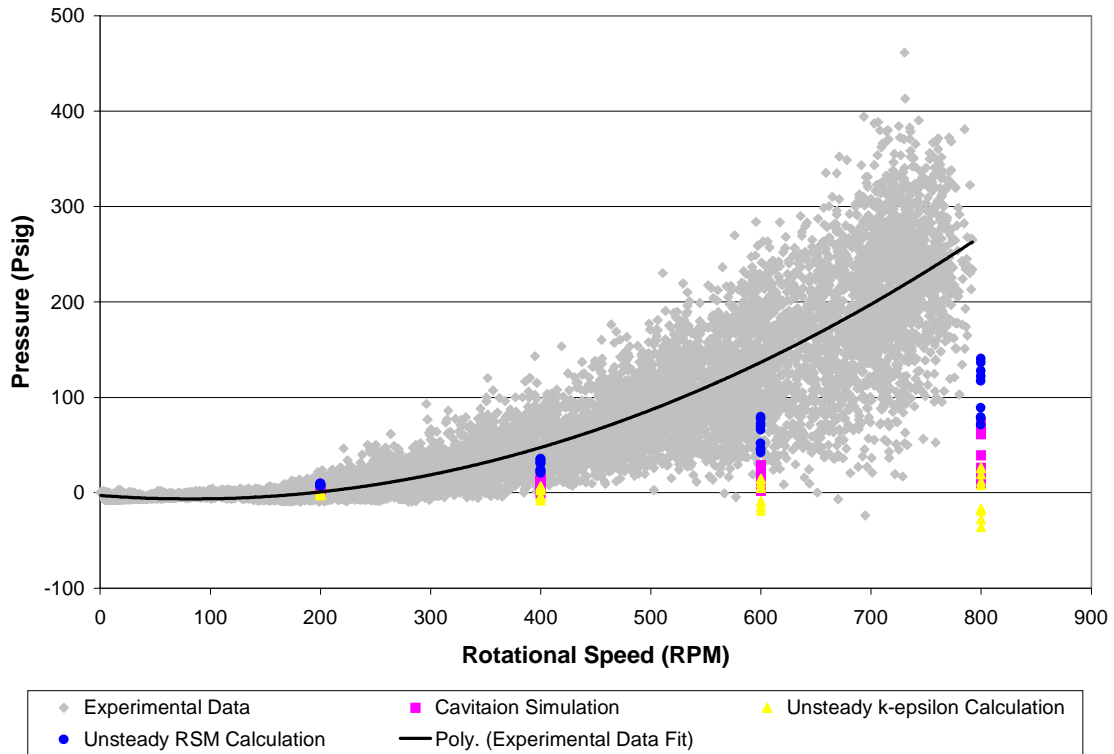


Figure 5.9 Pressure data comparison: pressure side, tip of stator blade

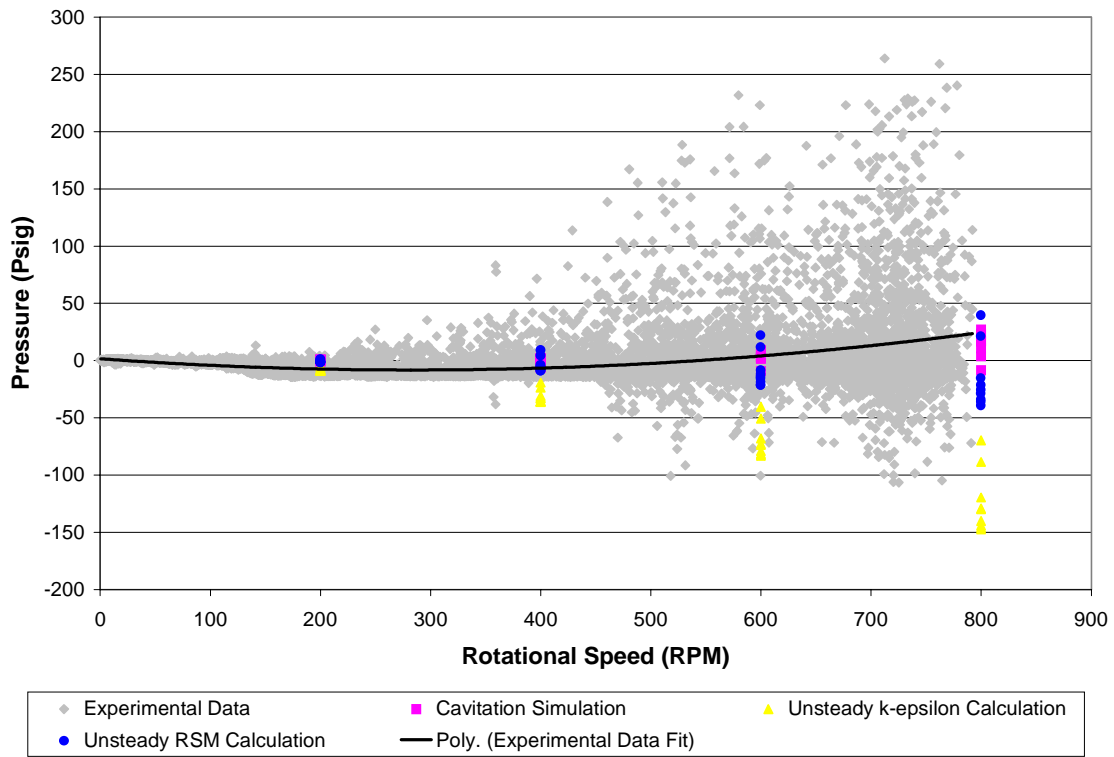


Figure 5.10 Pressure data comparison: suction side, tip of stator blade

One can clearly see the dramatic difference in the pressure data at the blade tip region from the figures discussed previously. The trendline passes nicely through the pressure data of the CFD simulations, with the exception of the unsteady $k-\varepsilon$ calculation, for the suction side. On the other hand, the calculated pressure data are much lower than the experimental data for the pressure side. Even though the unsteady RSM calculation provides the best estimation of the three cases, it is still much lower than the experimental data. For example, for the 600 rpm data the mid-span value is approximately 65-70 psig while the trendline value is about 135-140 psig. Compared to Figure 5.7 at the hub the underestimation is about 45 psig only; and compared to Figure 5.10 the mid-span value of the calculated pressure is almost the same as the trendline value.

Such substantial underestimation of pressure on only one side would certainly lead to a considerable error when performing torque calculation. In this case, this would lead to a much lower torque than the experimental value because the pressure on the pressure side is underestimated. Furthermore, not only the inaccurate pressure difference would cause the calculated torque to be lower. The fact that the region in discussion is the tip region implies that the moment arm is longer and any error in the pressure difference will be aggravated in the torque calculation.

The fact that pressure data on the pressure side of the blade at both tip and hub are underestimated means that the dynamic pressure build-ups in these regions with more geometry boundaries have not yet been captured fully. In fact, due to the close confines of the geometry, the suction side at the hub is also subject to the dynamic pressure build-up. While the experimental pressure data provided are on the stator surface only and the accuracy is subject to the degree of the mechanical vibration, the analysis provides more information on where the possible inadequacy of the model lies.

Another investigation of the experimental pressure data is an approximation of the torque. By using a polynomial fit to represent the experimental pressure data along the blade span, one can integrate the pressure difference to obtain the torque. Table 5.6 lists the values of the torque from the integration using a second order polynomial fit.

Table 5.6 Integration of the pressure differences

Speed	(rpm)	200	400	600
Experimental Value	(N-m)	8400	33600	75600
Experimental Pressure Integration	(N-m)	3116	18972	67590
Unsteady RSM Calculation	(N-m)	5723	25142	50930
Unsteady RSM Pressure Integration	(N-m)	5054	15093	42138

Because in actual operation the rotational speed of the energy absorber does not reach 800 rpm, there is no available experimental pressure data to perform the integration. From the table, one can clearly see that the torque obtained from the integration of experimental pressure data is lower than the experimental torque value, measured on the rotor shaft. This is expected because the experimental pressure data available are on the surface of the stator only and the pressure profiles on the rotor surfaces cannot be represented accurately with this pressure distribution.

However, comparing the predicted torque and the torque calculated from the integration of the pressure differences in unsteady RSM calculation, a similar underestimation is evident. This suggests that a correlation to qualitatively, if not quantitatively, represent the actual torque with the simplified integration does exist. It is also clear that because such correlation exists, any improvement in the pressure distribution will not only contribute to the simplified integration of pressure differences, but also to the torque prediction.

From the pressure analysis, it is evident that the calculated pressure distribution of the CFD simulation is not accurate enough; and any improvement in the torque prediction requires a better representation of the pressure profile. Clearly, an unsteady calculation utilizing the Sliding Mesh Technique to fully simulate the dynamic change in the flow field may be the necessary configuration to correctly predict the torque.

5.7 SUMMARY

By utilizing different techniques, several interesting points appeared in the results and provide more information on the flow field in the energy absorber.

First, the dynamic effect can not be captured with the steady-state calculation. Certain characteristics of the flow field are not evident or not shown in the steady-state calculation while they can be observed in the results of the unsteady calculations. Also, the predicted torque of the unsteady calculations is much higher than the result of steady-state calculation, even though the Multiple Reference Frames model used in the calculation incorporates certain steady-state assumption.

The suspected cavitation, if it exists, does not have strong influence on the flow field. The results of both cavitation simulations and unsteady RSM calculations clearly indicate that the reason behind the problem of unrealistic pressure is more likely due to the modeling techniques rather than the modeling assumptions. The inadequacy of the standard $k-\varepsilon$ model when proper boundary conditions can not be set is found to be the major factor.

The calculated torque of the unsteady RSM calculation is approximately 70% of the experimental data. Through the analysis of the pressure data and the experimental data, indications are found that dynamic effects have not yet been captured fully and may be responsible for the underestimation.

Also, although the limitations in the FLUENT code restrain the possible combinations of the modeling techniques used, comparing the different results it is clear that the unsteady calculation employing the RSM turbulence model and MRF techniques provides the best approximation of the flow field.

6.0 Conclusions and Recommendations

6.1 CONCLUSIONS

In this work, computational fluid dynamics simulations have been performed in order to investigate the performance of a hydraulic energy absorber. The simulations were performed using the FLUENT CFD package. In order to reduce the computational resources required, a structured grid was created and the Multiple Reference Frames technique was used as the workhorse to simulate the interaction between the rotor and the stator. Three distinct cases have been set up to study the impact of various modeling techniques on the accuracy of the simulation.

In the cavitation simulation, steady-state calculations with the standard $k-\varepsilon$ turbulence model and two-phase model were performed. The results showed that physical cavitation is much less than suspected, or does not exist at all. The main reason behind the problem of unrealistically low pressures was because proper boundary conditions for the standard $k-\varepsilon$ model can not be set.

In the unsteady $k-\varepsilon$ calculation, unsteady calculations with the standard $k-\varepsilon$ turbulence model and one-phase model were performed. Dynamic effects, such as the passing of the blades, were captured to a certain degree in addition to the secondary flows, detached flows and recirculating flows that had been found in the steady-state simulations. By using the standard $k-\varepsilon$ turbulence model alone, the problem of the unrealistic pressure aggravated and again showed its inadequacy.

In the unsteady RSM calculation, unsteady calculations with the Reynolds Stress Model and one-phase model were performed. The implementation of the sophisticated turbulence model reduced the problem of the unrealistic pressure dramatically. The discovery strengthened the observation that employing the standard $k-\varepsilon$ model without setting proper boundary conditions is the major factor behind the problem.

The calculated torque values depended on whether the calculation was unsteady or steady. Results of the unsteady calculations are approximately 60%~70% of the experimental data, while those of steady-state calculations are only approximately 25%~30% of the experimental data. The unsteady RSM calculation provided better approximation in both pressure distribution and calculated torque than the other two cases. Analysis of the variation of the calculated torque with time and the pressure data showed that dynamic effects are the major factor in predicting the torque and have not yet been captured fully.

This study provided better understanding of the flows within the energy absorber and the necessary modeling assumptions and techniques to correctly simulate the flows. While there was still room for improvement in the results, all calculations were done with little additional computer resources. With the experimental data difficult to obtain, the results of the CFD simulations are valuable for any further investigation of the energy absorber.

6.2 RECOMMENDATIONS

The purpose of this research was to test the influence of different modeling technique to improve the CFD simulation of the energy absorber. From the various cases tested, the comparison of the results provided some recommendations for the future work.

The flow field within the energy absorber is very complex and highly dynamic due to the close coupling between the geometrical components, and steady-state assumptions may not be appropriate. Therefore, it is necessary to perform unsteady calculations in the future study. Also, the unsteady calculations in this study were done with the Multiple Reference Frames technique due to hardware constraint and its compatibility with the desired models to be tested. However, the results clearly showed that unsteady calculations with the Sliding Mesh Technique are necessary to eliminate the error resulting from the steady-state assumptions of the MRF model if further improvements are to be achieved.

Another important issue is the inadequacy of the standard $k-\varepsilon$ turbulence model because proper boundary conditions can not be set. Sophisticated turbulence model, such as the Reynolds Stress Model used in this investigation, are necessary to capture the flow. The multiple-phases model to simulate the cavitation would also be beneficial but may not be necessary, however, since the results did not indicate a high degree of the physical cavitation.

The experience in this study also showed that the integration of needed techniques may be challenging. As discussed previously, in the FLUENT code the Sliding Mesh Technique can not be used in conjunction with either the RSM turbulence model or the Eulerian Multiple Phases Model in structured grid calculations. An option for future structured-grid calculations is to employ the ReNormalization Group (RNG) $k-\varepsilon$ turbulence model and the Volume of Free-surface multiple-phases model. Both models

are not particularly suited for the flows within the energy absorber, but both can be used in conjunction with the other and the Sliding Mesh Technique.

Another option is to go back to unstructured grid calculations. Although this requires much more computational cost, the fact that the unstructured-grid calculation is gaining in popularity means that the unstructured grid portion of the FLUENT code, FLUENT 5.0, is more mature. As mentioned previously, the incompatibility between the Sliding Mesh Technique and the RSM turbulence model does not exist in the FLUENT 5.0. In fact, there are more turbulence models to choose from, among them the Realizable $k-\varepsilon$ turbulence model to address the inconsistency with the physics of the turbulent flows of both standard $k-\varepsilon$ model and RNG $k-\varepsilon$ model. Also, a dedicated cavitation model is provided in FLUENT 5.0. Furthermore, these models have fewer restrictions and can work in conjunction with most of the models available.

With the proper integration of these modeling techniques, more accurate results should be achieved and provide more information of the actual flow field. Once the results of the CFD calculation can be validated by or correctly correlated with the experimental data, numerical simulation can be introduced into the design or the performance prediction of the energy absorber.

7.0 References

- [1] Brothel, C., *Development of Computational Fluid Dynamics Modeling of High Energy Absorber*, Diploma Project, Swiss Federal Institute of Technology of Lausanne, Switzerland, 1998.
- [2] Numazawa, A., Ushijima, F., Kagenoni, G. J., and Ishihara, T., *An Experimental Analysis of Fluid Flow in a Torque Converter*, SAE Paper No. 830571, 1983
- [3] Fujitani, K, Himeno, R., and Takagi, M., *Computational Study on Flow through a Torque Converter*, SAE Paper No. 881746, 1988.
- [4] Bahr, H. M., Flack, R.D., By, R. R. and Zhang, J. J., *Laser Velocimeter Measurements in the Stator of a Torque Converter*, SAE Paper No. 901769, 1990.
- [5] By, R. R., and Lakshminarayana, B., *Static pressure Measurements in a Torque Converter Stator*, SAE Paper No. 911934, 1991.
- [6] Abe, K., Kondoh, T., Fukumura, K., and Kojima, M., *Three-Dimensional Simulation of the Flow in a Torque Converter*, SAE Paper No. 910800. 1991.
- [7] By, R. R., Kuntz, R. F., and Lakshminaranaya, B., *Navier-Stokes Analysis of the Pump Flow Field of an Automotive Torque Converter*, ASME FED Vol. 154, Pumping Machinery, 265-274, 1993.
- [8] Schulz, H., Greim, R., and Volgmann, W., *Calculation of Three-Dimensional Viscous Flow in Hydrodynamic Torque Converters*, ASME Paper 94 – GT – 208, 1994.
- [9] Placek, J. and Tavlarides, L. L., *Turbulent Flow in stirred tanks, Part I: Turbulent Flow in the Turbine Impeller Region*, A. I. Ch. E. J. Vol. 31(7), 1130-1120, 1985.
- [10] Placek, J., Tavlarides, L. L., Smith, G. W. and Fo• t, I., *Turbulent Flow in stirred tanks, Part II: A Two-Scale Model of Turbulence*, A. I. Ch. E. J. Vol. 32(11), 1771-1786, 1986.
- [11] Torvik, R. and Svendsen, H. F., *Modelling of Slurry Reactors. A Fundamental Approach*, Chem. Engng Sci. Vol. 45(8), 2325-2332, 1990.
- [12] Kresta, S. M. and Wood, P. E., *Prediction of the Three-dimensional Turbulent Flow in Stirred Tanks*, A. I. Ch. E. J. Vol. 37(3), 448-460, 1991.

- [13] Gosman, A. d., Lekakou, C., Politis, S., Issa, R. I., and Looney, M. K., *Multidimensional modeling of Turbulent Two-Phase Flows in Stirred Vessels*, A. I. Ch. E. J. Vol. 38(12), 1946-1956, 1992.
- [14] Takeda, H., Narasaki, K., Kitajima, H., Sudoh, S., Onofusa, M., and Iguchi, S., *Numerical Simulation of Mixing Flows in Agitated Vessels with Impellers and Baffles*, Computers Fluids Vol. 22(2/3), 223-228, 1993.
- [15] Morud, K. E. and Hjertager, B. H., *LDA Measurements and CFD modelling of Gas-Liquid Flow In a Stirred Vessel*, Chemical Engineering Science Vol. 51(2), 233-249, 1996.
- [16] Fluent Inc., Lebanon, NH, 1997.
- [17] Fluent Inc., *Fluent 4.4: User's Guide Vol. 4*, Lebanon, NH, 1997.
- [18] Hinze, J. O., *Turbulence*, McGraw-Hill Publishing Co., New York, NY, 1975.
- [19] Launder, B. E. and Spalding, D. B., *Lectures in Mathematical Models of turbulence*, Academic Press, London, England, 1972.
- [20] Launder, B. E. and Spalding, D. B., *The Numerical Computation of Turbulent Flows*, Computer Methods in Applied Mechanics and Engineering, Vol. 3, 269-289, 1974.
- [21] Launder, B. E., Reece, G. J., and Rodi, W., *Progress in the Development of a Reynold-Stress Turbulence Closure*, J. Fluid Mech., Vol. 68, 537-566, 1975.
- [22] Launder, B. E., *Second-Moment Closure: Present... and Future?*, Iunter. J. Heat Fluid Flow, Vol. 10(4), 282-300, 1989
- [23] Daly, B. J. and Harlow, F. H., *Phys. Fluids*, Vol. 13, 2634-2649, 1970.
- [24] Rodi, W., *Turbulence Models and their Application in Hydraulics*, Delft, The Netherlands, IAHR, 1984.
- [25] Lien, F. S. and Leschziner, M. A., *Assessment of Turbulence-Transport Models Including Non-Linear RNG Eddy-Viscosity Formulation and Second-Moment Closure for Flow Over a Backward-Facing Step*, Computers Fluids, Vol. 23(8), 983-1004, 1994.
- [26] Thompson, J. F., Warsi, Z. U. A., and Mastin, C. W., *Numerical Grid Generation*, North-Holland, NY, 1985.

- [27] Boysan, Dr. F., *A Two-Fluid Model for FLUENT*, Flow Simulation Consultants Ltd., Sheffield, England, 1990.
- [28] Fluent Inc., *Fluent 4.4: User's Guide Vol. 2*, Lebanon, NH, 1997.

8.0 Appendix A – STRUCTURED GRID DETAILS

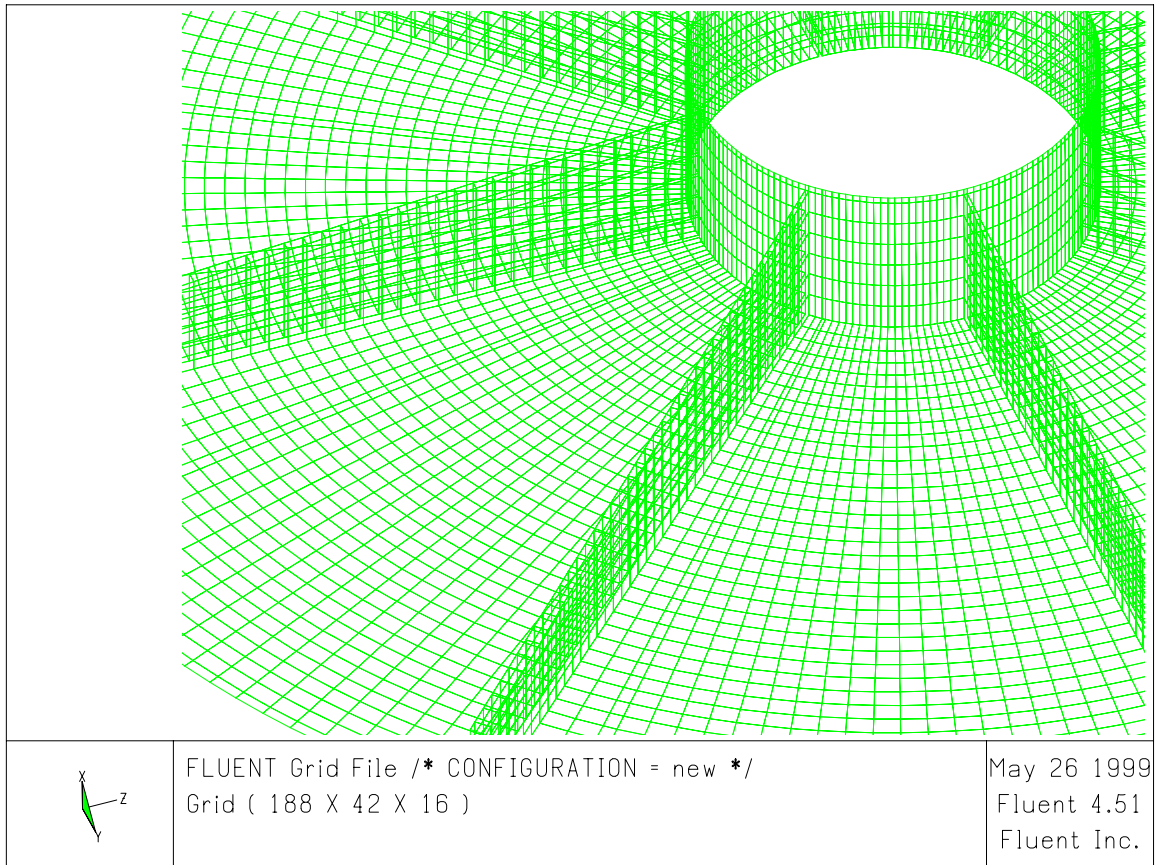


Figure A.1 Rotor grid detail

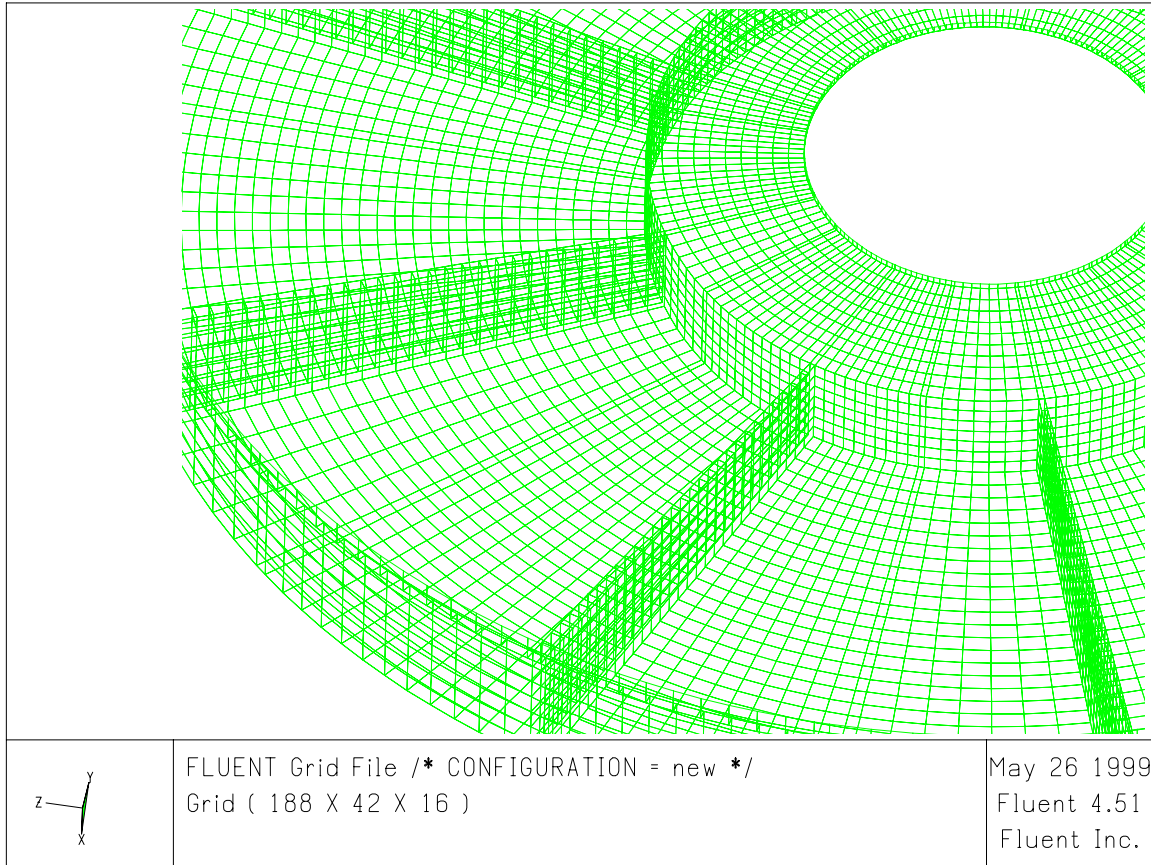


Figure A.2 Stator grid detail

9.0 Appendix B – REFINED STRUCTURED GRID

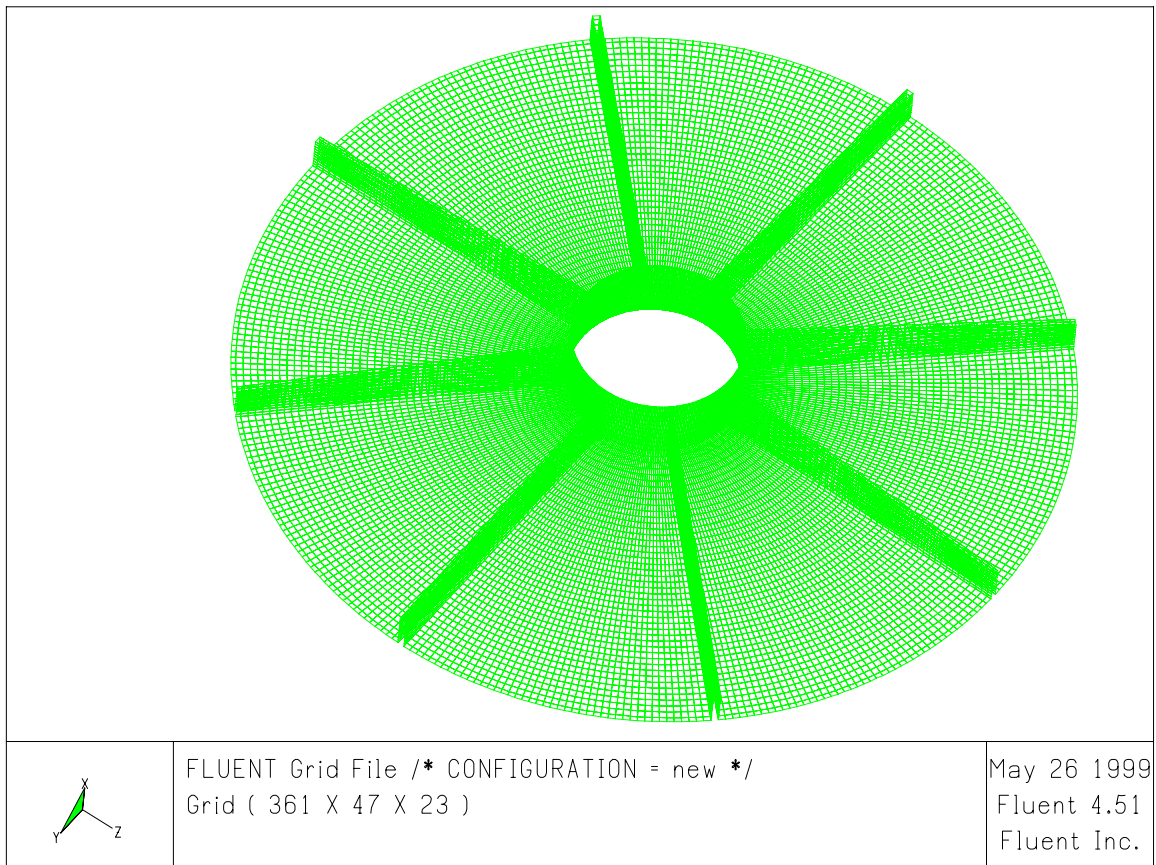


Figure B.1 Refined rotor surface grid

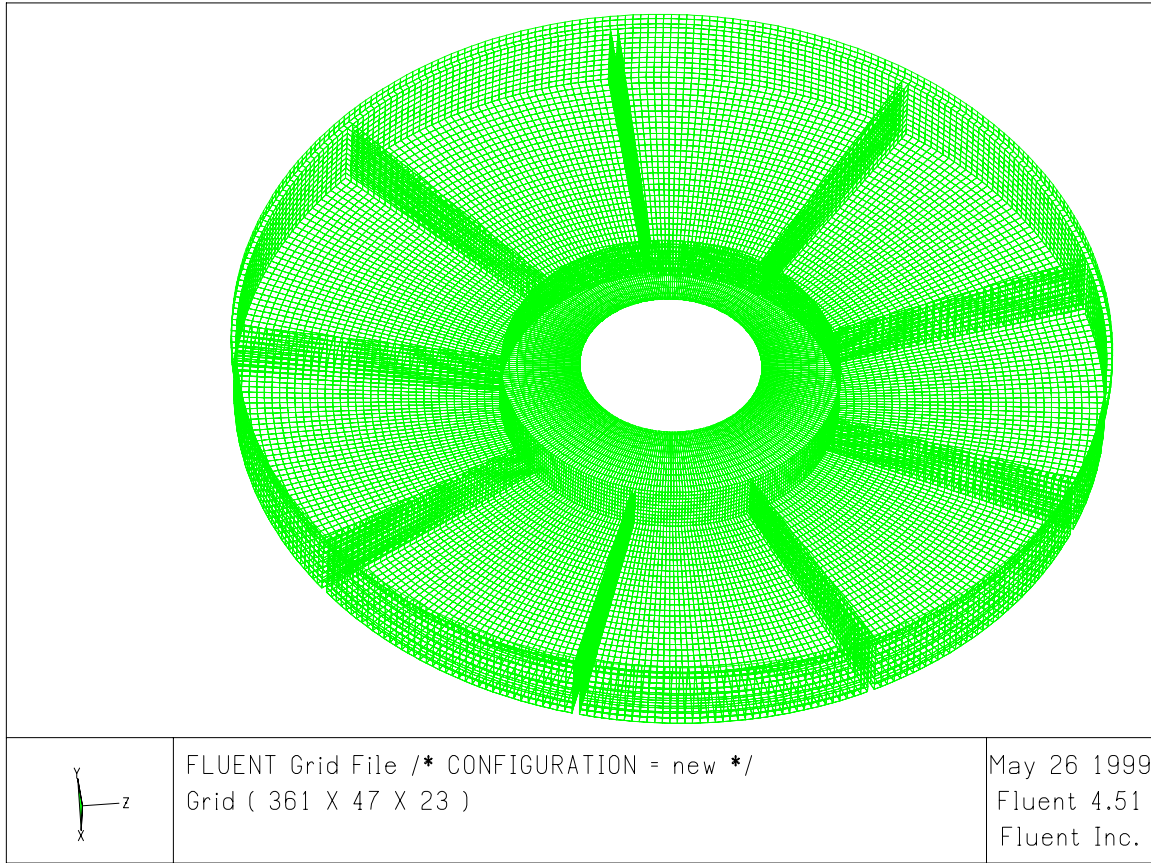


Figure B.2 Refined stator surface grid

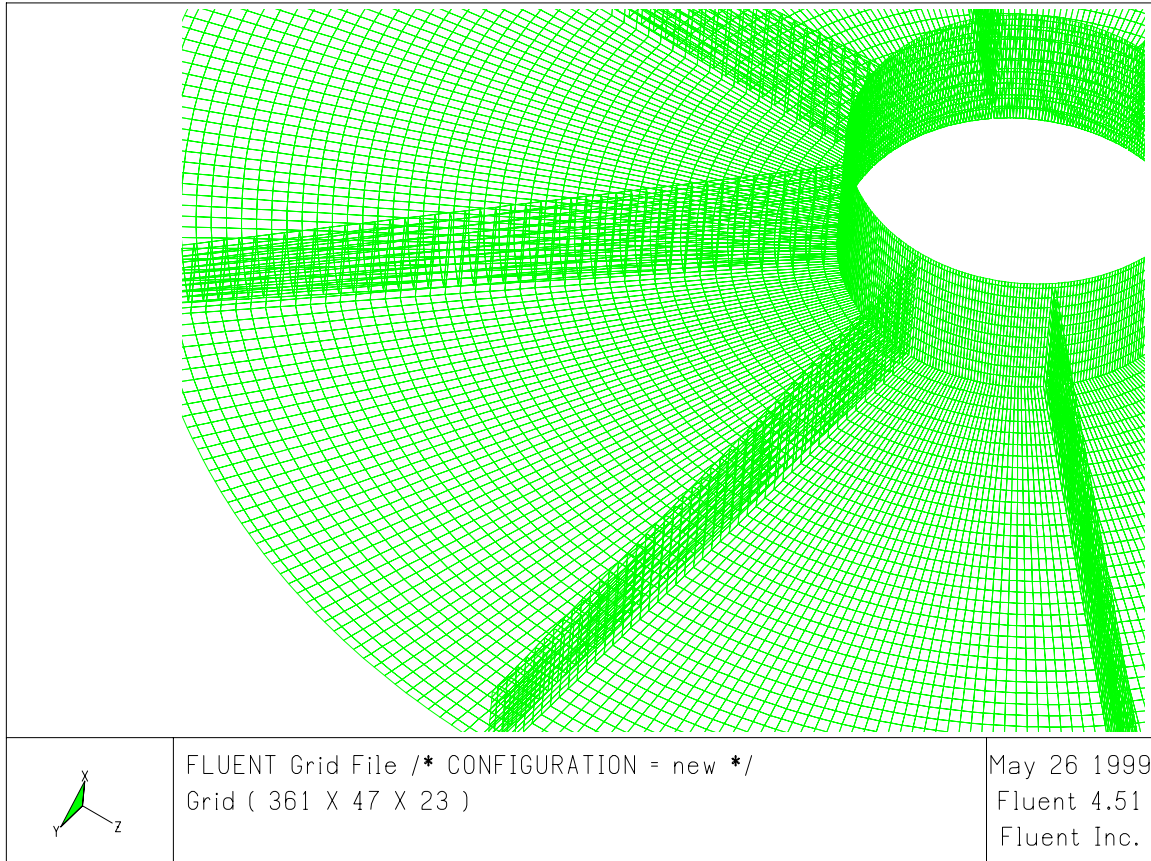


Figure B.3 Refined rotor grid detail

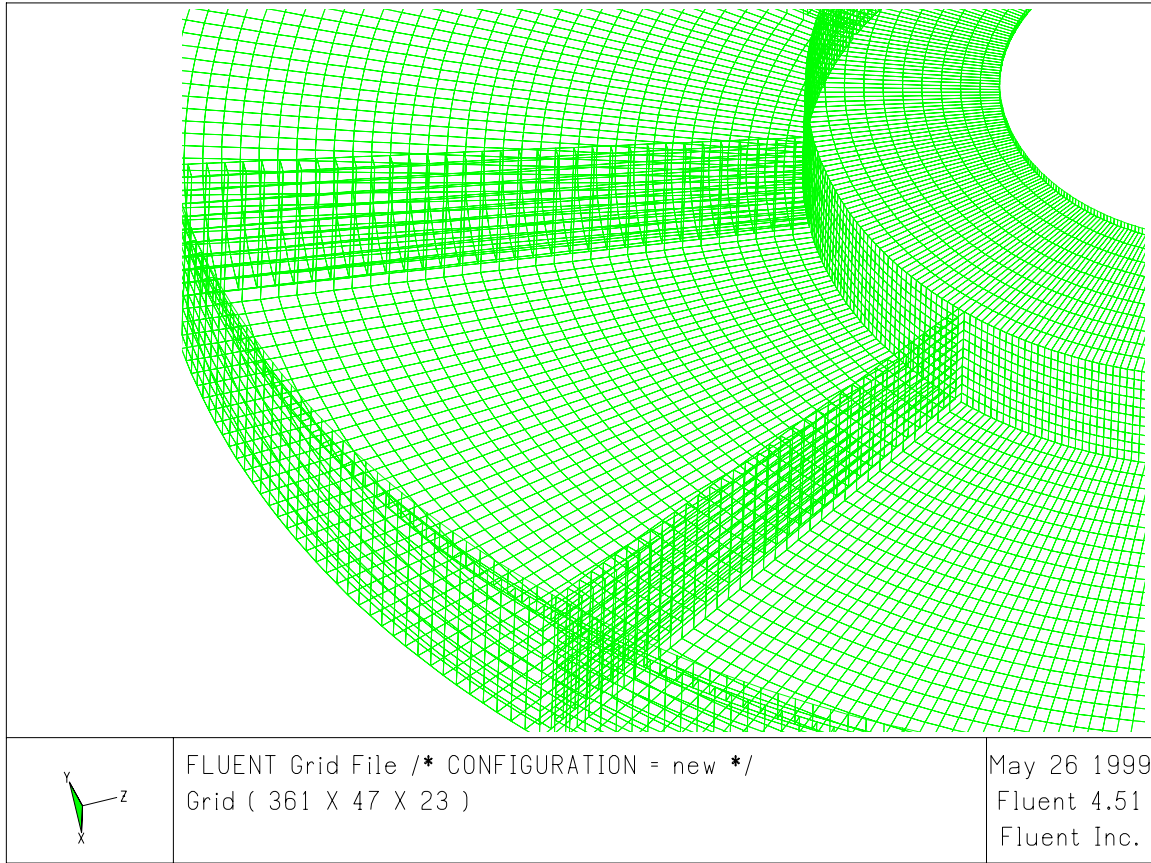


Figure B.4 Refined stator grid detail